

# Flutter in Functionally Graded Conical Shell under Follower Force

Rupsagar Chatterjee<sup>1</sup>, Sudib Kumar Mishra<sup>2</sup>

1- Associate Engineer, Airbus Group India Private Limited, Bangalore

2 - Professor, Department of Civil Engg., Indian Institute of Technology Kanpur, UP

**ABSTRACT:** Truncated conical shells are essential components of rocket booster nozzles and thrust vector control (TVC) systems for propulsion of multi-stage launch vehicles. The TVCs assist the ascent of launch vehicles by directing the resultant thrust from the boosters, acting as a follower force that might trigger instability. Previous studies on instability are mostly limited to cylindrical shell geometry. This study presents the analysis of a truncated conical shell under follower force of constant magnitude, considering thickness-wise gradation of elastic properties, as employed for thermal management. The governing equations are derived following the Hamilton's principle, considering first-order shear deformation and solved using finite element method, approximating the circumferential displacements by harmonic functions. Clamped and free boundaries are assumed at the small and large ends, respectively. Influence of mass and stiffness proportional damping are considered. Although strong flutter appears as the dominant instability mode; instances of erratic weak instabilities are also observed for undamped and lightly damped cases. Long shells with small semi-vertex angles are noted to be less susceptible to weak instability but exhibit much lower flutter load. The non-dimensional flutter load attains saturation in long shells with small semi-vertex angle beyond a thickness parameter. The critical load decreases monotonically for increasing slenderness, except for small semi-vertex angles and thickness parameter greater than 0.1, for which, it increases shortly before reduction. The flutter loads for undamped and lightly damped cases are highly sensitive to changing geometry. Although damping enhances the stability, its effect gets saturated. The flutter loads are presented for varying non-dimensional parameters, characterizing the shell geometry and material properties.

**Keywords:** Functionally Graded Material, Truncated Conical Shell, Follower Force, Flutter, Finite Element Method

**Correspondence to:** Sudib Kumar Mishra; **E-mail:** smishra@iitk.ac.in

## 1. Introduction

Shells are widely used in engineering because of their efficient load-carrying behavior, high strength-to-weight ratio and the ability to contain space by virtue of their geometry. Shells find wide applications as storage structures, containment for nuclear power plants, domes, pressure vessels, aircraft propulsion systems, fuselages, rockets, missiles, ships and submarines. Many biological lifeforms such as plants, animals and human organs (eye, skull, bones and joints) are inherently shell structures.

Over the past century, researchers have put forward various theories of shells. These include significant contributions by Sanders (1959), Novozhilov (1964), Vlasov (1964), Flügge (1966) and many others. These works are commonly referred as classical shell theories, in which, the displacement fields are approximated by the Kirchhoff-Love hypothesis with thin shell assumptions. Leissa (1993) provided a comprehensive study of various thin shell theories applied to different shell geometries. Contrary to the theories of thin shells, thick shell theories consider the effect of transverse shear deformations and rotary inertia. The rotations of the normal to the surface are considered in addition to the displacement components.

Functionally graded materials (FGMs) are an advanced class of inhomogeneous composite materials. Unlike conventional composites, the mechano-thermal properties of FGMs vary smoothly across the thickness. This gradual change of properties alleviates several difficulties associated with the conventional materials. FGMs have found widespread applications as super heat-resistant refractory materials in spacecraft (Koizumi and Niino 1995; Koizumi 1997). Functionally graded shells have gained prominence in recent years as a viable structural material for use in launch vehicles, owing to the feasibility of creating thermal barrier in structures exposed to high-temperature gradient.

FGM truncated conical shells are one of the essential structural components in the propulsion system of launch vehicles. In present-day multi-stage launch vehicles, they find extensive use as rocket booster nozzles and thrust vector control (TVC) systems. After the propellant combustion in booster engines, the nozzle extension at the rear end of the launch vehicle discharges the exhaust to generate the required thrust for lift-off and subsequent flight of the vehicle. During this operation, high pressure acts on the nozzle, causing elastic deformations in its body. These deformations change the direction of the generated thrust from the boosters. Of course, the TVCs assist in sophisticated maneuvering in the flight path

during the ascent of the launch vehicle by appropriately directing the resultant thrust from the boosters. Nevertheless, a follower force acts on the nozzle.

Early works on truncated conical shells mainly dealt with the free vibration analysis using different analytical and numerical techniques by adopting alternative choice of material properties. These include works by Irie et al. (1984), Kayran and Vinson (1990), Tong (1993), Shu (1996), Liew et al. (2005) and many others. Bhangale et al. (2006) studied the linear thermoelastic buckling and free vibration characteristics of a first-order shear deformable FG truncated conical shells subjected to high-temperature environment. The finite element approach was used for analysis. Tornabene et al. (2009) presented the free vibration analysis of FG conical and cylindrical shells and annular plates employing moderately thick shell assumptions. Malekzadeh et al. (2012) studied the three-dimensional free vibration of FGM truncated conical shells subjected to thermal environment using the differential quadrature method (DQM).

Later, several studies have been conducted on flutter instability of functionally graded plates and shells in supersonic airflow. Ibrahim et al. (2008) presented the flutter and post-buckling behavior of functionally graded rectangular plates using nonlinear finite element analysis considering thermal effects and aerodynamic pressure, using thin plate assumption. In another work, Ibrahim et al. (2009) also studied the flutter phenomenon in thin rectangular FGM plates using nonlinear finite element method under the combined effect of supersonic airflow, thermal and random acoustic loads. Mahmoudkhani et al. (2010) determined the aeroelastic stability boundaries of simply supported FGM conical shells subjected to supersonic flow under thermal environment. Sabri and Lakis (2013) put forward a hybrid finite element formulation based on Sanders thin shell theory and finite element method to predict flutter in FGM cylindrical shells under supersonic airflow. Su et al. (2019) developed a unified approach for the vibration and flutter analysis of elastically restrained first-order shear deformable stiffened FGM plates. Wei et al. (2020) studied the flutter behavior of axially functionally graded (AFG) cylindrical shells. It was shown that such structures could have superior aeroelastic qualities with judicious choice of parameters. Sun et al. (2021) argued that the aeroelastic stability of systems could be improved against flutter by adding lumped masses, which may be an effective design methodology for the AFG panels. Muc and Flis (2021) presented free vibration and flutter behavior for porous functionally graded rectangular plates using analytical and Rayleigh-Ritz methods. Zhou et al. (2021) presented the free vibration and flutter characteristics of graphene platelet (GPL) reinforced porous

FGM cylindrical panels. AminYazdi (2021) performed flutter analysis of functionally graded carbon nanotubes (FG-CNTs) reinforced double-curved shells with geometric imperfections.

In the context of shells with follower force, Park and Kim (2000) studied the dynamic instability of a free-free cylindrical shell with first-order shear deformation theory (FSDT). Torki et al. (2014a) performed a dynamic instability analysis of cantilever FGM cylindrical shells subjected to follower force. In another study Torki et al. (2014b) investigated the flutter of cantilever FGM cylindrical shells considering uniformly distributed and linearly increasing follower forces.

It is evident from the ongoing discussion that though the behavior of space launching structures have been idealized as cylindrical shells and beams under follower force in previous investigations, a lacuna exists in the study of stability characteristics of truncated conical shells subjected to follower force. The present study aims to address this research gap. This study presents the stability behavior of FG truncated conical shells subjected to follower force of constant magnitude. The study accommodates varying geometry of the shells by adjusting their semi-vertex angle, slant height, radius and thickness. Varying characteristics of the material properties (namely, the damping, functional gradation exponent and so on) for the shell are included in the analysis in order to study their influences on the stability against flutter.

## 2. Formulation of the governing equations

The geometry of a truncated conical shell is shown in *Figure 1*. In this figure,  $\alpha$  refers to the semi-vertex angle of the complete cone. The coordinate system is taken in a way, such that the  $s$  coordinate axis runs along a meridian starting from the apex of the cone to the larger base and acts as a generator of the surface. The angular coordinate  $\theta$  runs circumferentially at any section from a reference meridian. The direction normal to both  $s$  and  $\theta$  is taken to be the  $z$  direction and is taken positive outward from the shell middle surface. The shell is assumed to have constant thickness  $h$ . The  $s$  coordinates of the smaller and larger ends of the shell are taken as  $s_1$  and  $s_2$  respectively, and respective radii are denoted by  $r_1$  and  $r_2$ . The symbol  $l$  is the slanted height of the frustum. The radius  $r$  of the mid-surface ( $z = 0$ ) at any distance  $s$  from the apex of the cone is then given as,

$$r(s) = s \sin \alpha \quad (1)$$

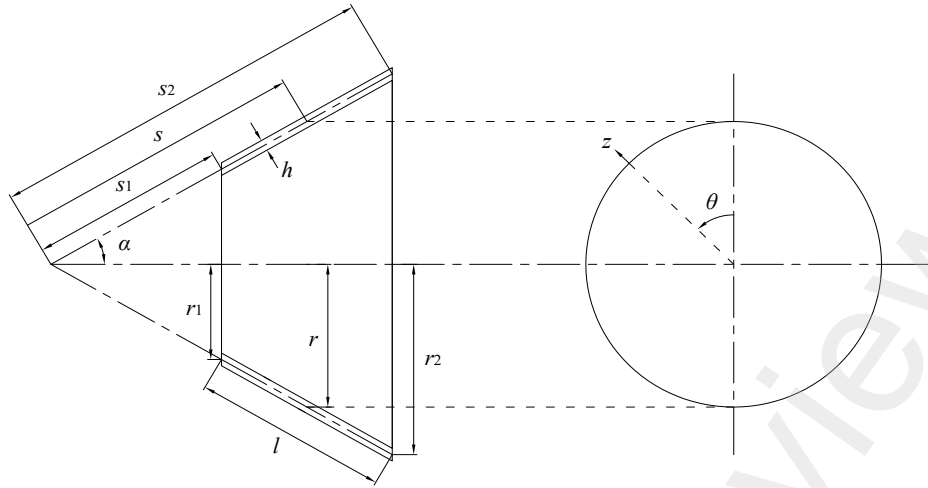


**Figure 1** Geometry of a truncated conical shell, along with the reference coordinate system

For studying the dynamic stability, the smaller end of the conical shell is assumed to be clamped whereas the larger end is kept free. The larger end is subjected to a uniformly distributed follower force of constant intensity  $P$ , shown in *Figure 2*. This force is assumed to be acting along the mid-surface of the shell and remains tangential to the meridian at all points on the edge at any configuration of the shell. Thus, the direction of the follower force at any two diametrically opposite points on the free edge would not be parallel due to the conical shape of the shell, which is unlike the case of a cylindrical shells, for which the meridians are parallel to the surface generator.

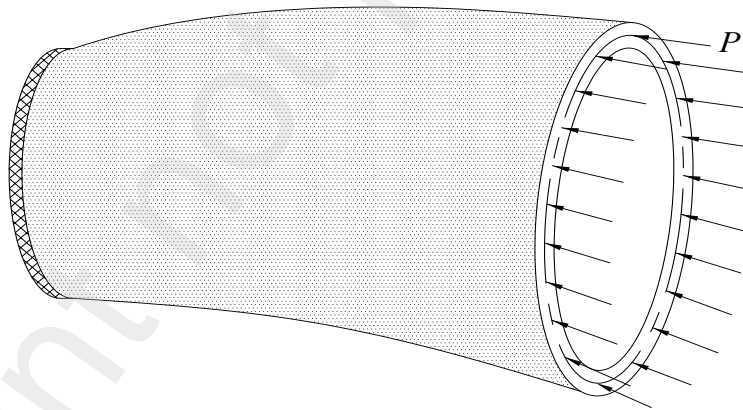


**Figure 2** Truncated conical shell with clamped small end and free large end subjected to uniformly distributed follower force along the mid-surface of the larger edge

The density, Young's modulus and Poisson's ratio for the FG shell at any depth  $z$  from the mid-surface are denoted by  $\rho$ ,  $E$  and  $\nu$  respectively. The Poisson's ratio for the FGM is reasonably assumed to be constant to avoid complexity (Reddy 2000). However, the density and Young's modulus vary continuously across the thickness of the shell. As such, these quantities for the homogeneous constituent of the FGM are added with subscripts  $i$  and  $o$  (i.e.  $\rho_i$ ,  $E_i$ ,  $\rho_o$  and  $E_o$ ) to represent the properties at the inner and outer shell surfaces,

respectively. In this study, two FGM models are considered for the truncated conical shell, namely, power-law type FGM (PFGM) and the exponential FGM (EFGM) (Chi and Chung 2006).

The material properties vary as a power-law function of the volume fraction of the constituents in PFGM. Depending on the surface of choice, from where the volume fraction is controlled, alternative formulations can be found in the literature (Tornabene et al. 2009). In this work, the volume fraction of the inner surface constituent at any depth  $z$  is taken as,

$$V_i(z) = \left( \frac{1}{2} - \frac{z}{h} \right)^\eta \quad (2)$$

The total volume fraction of the inner and outer surface constituents at any depth within the shell is always unity. That is,

$$V_i(z) + V_o(z) = 1 \quad (3)$$

where  $V_o$  is the volume fraction of the outer surface constituent. Using the rule of mixtures, the density and Young's modulus at any point in the PFGM becomes,

$$\rho(z) = \rho_i V_i(z) + \rho_o V_o(z) = \rho_i \left( \frac{1}{2} - \frac{z}{h} \right)^\eta + \rho_o \left\{ 1 - \left( \frac{1}{2} - \frac{z}{h} \right)^\eta \right\} \quad (4)$$

$$E(z) = E_i V_i(z) + E_o V_o(z) = E_i \left( \frac{1}{2} - \frac{z}{h} \right)^\eta + E_o \left\{ 1 - \left( \frac{1}{2} - \frac{z}{h} \right)^\eta \right\} \quad (5)$$

where the volume fraction index  $\eta$  ( $0 \leq \eta < \infty$ ) determines the variation profile of the constituent materials. For  $\eta = 0$ , the PFGM shell is completely composed of the inner surface material whereas, for  $\eta \rightarrow \infty$ , it is entirely composed of the outer surface material. Naturally, these cases represent the special case of a shell with homogeneous material. *Figure 3* shows the variation of  $V_i$  in PFGM with  $z/h$  for different values of  $\eta$ . In EFGM, the material properties between the two surfaces of a truncated conical shell vary exponentially as follows (Chi and Chung 2006),

$$\rho(z) = \rho_o e^{\left( \frac{1}{2} - \frac{z}{h} \right) \ln \left( \frac{\rho_i}{\rho_o} \right)} \quad (6)$$

$$E(z) = E_o e^{\left( \frac{1}{2} - \frac{z}{h} \right) \ln \left( \frac{E_i}{E_o} \right)} \quad (7)$$

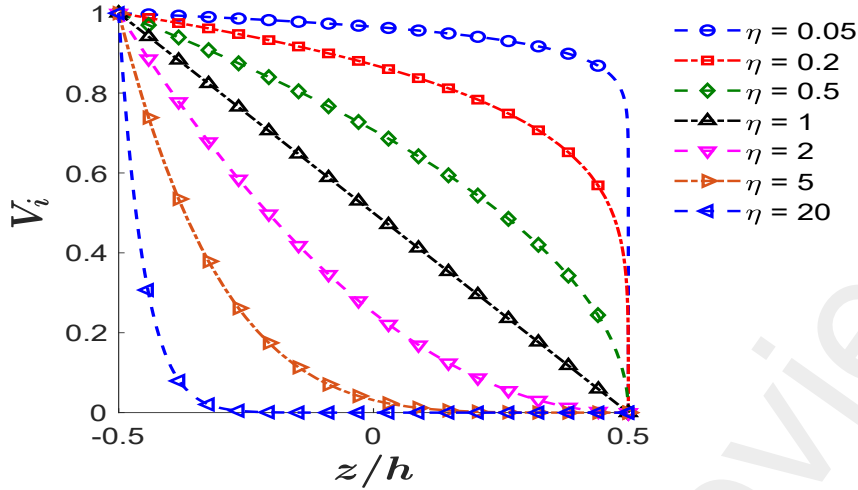


**Figure 3** Variation of  $V_i$  through the thickness for PFGM with different  $\eta$

A moderately thick shell is considered in the present work and therefore the Reissner-Mindlin first-order shear deformation theory (FSDT) is used for analysis. Based on the assumptions of the first-order shear deformation theory, the displacement components  $(\bar{u}, \bar{v}, \bar{w})$  at any point in the shell having coordinates  $(s, \theta, z)$  at time  $t$  is written as,

$$\bar{u}(s, \theta, z, t) = u(s, \theta, t) + z\phi(s, \theta, t) \quad (8.1)$$

$$\bar{v}(s, \theta, z, t) = v(s, \theta, t) + z\psi(s, \theta, t) \quad (8.2)$$

$$\bar{w}(s, \theta, z, t) = w(s, \theta, t) \quad (8.3)$$

where  $u$ ,  $v$  and  $w$  represent the displacement components of the shell middle surface in the  $s$ ,  $\theta$  and  $z$  directions respectively. The quantities  $\phi$  and  $\psi$  denote the rotations of the normal to the middle surface with respect to  $s$  and  $\theta$  directions, respectively. No shear correction factor is assumed in the analysis. Using (8.1) to (8.3), the strains at any point then becomes (Soedel 2004),

$$\boldsymbol{\varepsilon} = \boldsymbol{\Xi} \boldsymbol{\Delta} \quad (9)$$

where the strain vector  $\boldsymbol{\varepsilon}$ , generalized displacement vector  $\boldsymbol{\Delta}$  and the kinematic operator  $\boldsymbol{\Xi}$  are defined as,

$$\boldsymbol{\varepsilon} = [\varepsilon_{ss} \quad \varepsilon_{\theta\theta} \quad \varepsilon_{s\theta} \quad \varepsilon_{sz} \quad \varepsilon_{\theta z}]^T \quad (10)$$

$$\boldsymbol{\Delta} = [u \quad v \quad w \quad \phi \quad \psi]^T \quad (11)$$

$$\mathbf{\varepsilon} = \begin{bmatrix} \frac{\partial}{\partial s} & 0 & 0 & z \frac{\partial}{\partial s} & 0 \\ \frac{1}{s} & \frac{1}{s \sin \alpha} \frac{\partial}{\partial \theta} & \frac{1}{s \tan \alpha} & \frac{z}{s} & \frac{z}{s \sin \alpha} \frac{\partial}{\partial \theta} \\ \frac{1}{s \sin \alpha} \frac{\partial}{\partial \theta} & \frac{\partial}{\partial s} - \frac{1}{s} & 0 & \frac{z}{s \sin \alpha} \frac{\partial}{\partial \theta} & z \left( \frac{\partial}{\partial s} - \frac{1}{s} \right) \\ 0 & 0 & \frac{\partial}{\partial s} & 1 & 0 \\ 0 & -\frac{1}{s \tan \alpha} & \frac{1}{s \sin \alpha} \frac{\partial}{\partial \theta} & 0 & 1 \end{bmatrix} \quad (12)$$

Assuming linearly elastic, isotropic material property, the stress ( $\sigma$ ) - strain ( $\varepsilon$ ) relation can be written using the constitutive matrix ( $D$ ) as

$$\sigma = D\varepsilon \quad (13)$$

where,

$$\sigma = [\sigma_{ss} \quad \sigma_{\theta\theta} \quad \sigma_{s\theta} \quad \sigma_{sz} \quad \sigma_{\theta z}]^T \quad (14)$$

and, the constitutive matrix is given as,

$$D = \begin{bmatrix} \frac{E}{1-\nu^2} & \frac{\nu E}{1-\nu^2} & 0 & 0 & 0 \\ \frac{\nu E}{1-\nu^2} & \frac{E}{1-\nu^2} & 0 & 0 & 0 \\ 0 & 0 & \frac{E}{2(1+\nu)} & 0 & 0 \\ 0 & 0 & 0 & \frac{E}{2(1+\nu)} & 0 \\ 0 & 0 & 0 & 0 & \frac{E}{2(1+\nu)} \end{bmatrix} \quad (15)$$

Applying the Hamilton's principle, the equation of motion for the truncated conical shell subjected to follower force can be written as,

$$\int_{t_1}^{t_2} (\delta T - \delta U - \delta V + \delta W_{nc}) dt = 0 \quad (16)$$

where  $\delta T$ ,  $\delta U$ ,  $\delta V$  represent the variations of the kinetic energy, strain energy and potential energy due to the conservative part of the follower force, whereas  $\delta W_{nc}$  represents the virtual work done by the non-conservative part of the follower force, respectively (Kim



and Kim 2000; Park and Kim 2000; Simitses and Hodges 2006). Individual components in the integrand are obtained as,

$$\delta T = \int_0^{2\pi} \int_{s_1}^{s_2} \int_{-\frac{h}{2}}^{\frac{h}{2}} \rho \left\{ \begin{aligned} &\dot{u}\delta\dot{u} + \dot{v}\delta\dot{v} + \dot{w}\delta\dot{w} + z^2 (\dot{\phi}\delta\dot{\phi} + \dot{\psi}\delta\dot{\psi}) \\ &+ z (\dot{u}\delta\dot{\phi} + \dot{\phi}\delta\dot{u} + \dot{v}\delta\dot{\psi} + \dot{\psi}\delta\dot{v}) \end{aligned} \right\} (s \sin \alpha + z) dz ds d\theta \quad (17)$$

$$\delta U = \int_0^{2\pi} \int_{s_1}^{s_2} \int_{-\frac{h}{2}}^{\frac{h}{2}} \boldsymbol{\varepsilon}^T \mathbf{D} \boldsymbol{\varepsilon} (s \sin \alpha + z) dz ds d\theta \quad (18)$$

$$\delta V = P \int_0^{2\pi} \int_{s_1}^{s_2} \left( \frac{\partial w}{\partial s} \frac{\partial \delta w}{\partial s} + \frac{\partial v}{\partial s} \frac{\partial \delta v}{\partial s} \right) s \sin \alpha ds d\theta \quad (19)$$

$$\delta W_{nc} = P \int_0^{2\pi} \left[ \left( \delta w \frac{\partial w}{\partial s} + \delta v \frac{\partial v}{\partial s} \right) s \sin \alpha \right]_{s=s_2} d\theta \quad (20)$$

where  $(\dot{\phantom{x}})$  denotes differentiation with respect to time. The solution of the generalized displacements can be assumed in the following form (Bhangale et al. 2006),

$$u(s, \theta, t) = \sum_{n=0}^{\infty} e^{\Lambda t} \bar{U}(s) \cos n\theta \quad (21.1)$$

$$v(s, \theta, t) = \sum_{n=0}^{\infty} e^{\Lambda t} \bar{V}(s) \sin n\theta \quad (21.2)$$

$$w(s, \theta, t) = \sum_{n=0}^{\infty} e^{\Lambda t} \bar{W}(s) \cos n\theta \quad (21.3)$$

$$\phi(s, \theta, t) = \sum_{n=0}^{\infty} e^{\Lambda t} \bar{\Phi}(s) \cos n\theta \quad (21.4)$$

$$\psi(s, \theta, t) = \sum_{n=0}^{\infty} e^{\Lambda t} \bar{\Psi}(s) \sin n\theta \quad (21.5)$$

where,  $\bar{U}$ ,  $\bar{V}$ ,  $\bar{W}$ ,  $\bar{\Phi}$  and  $\bar{\Psi}$  are the shape functions of the respective displacement fields along the  $s$  direction and  $n$  denotes the circumferential wave number.

Hereafter, the finite element method is preferably used to solve the governing equations. A three-noded Lagrangian element is adopted for discretization of the truncated conical shell along the  $s$  coordinate. It may be noted that the approximation along the  $\theta$  coordinate leads to a ring element in the circumferential direction of the shell. Following the above, the generalized displacement vector is given as,

$$\Delta = \sum_{n=0}^{\infty} e^{\Lambda t} N^{(n)} \bar{\Delta} \quad (22)$$

where  $N^{(n)}$  is the shape function matrix in the  $n$ -th circumferential mode, which is a function of  $s$  and  $\theta$ ; the symbol  $\bar{\mathbf{A}}$  is the generalized nodal displacement vector at the shell mid-surface in the discretized geometry. Using (22), the expression for strain in (9) becomes,

$$\boldsymbol{\varepsilon} = \sum_{n=0}^{\infty} e^{\Lambda t} \boldsymbol{\Xi} N^{(n)} \bar{\mathbf{A}} = \sum_{n=0}^{\infty} e^{\Lambda t} \mathbf{B}^{(n)} \bar{\mathbf{A}} \quad (23)$$

It can be seen from (17) to (20) that the shape functions are mutually orthogonal with respect to the circumferential bases. This is true for shells with axisymmetric geometry and boundary conditions (Leissa 1993). Since the equations hold true for any arbitrary circumferential mode, they can be solved separately for each  $n$ . Thus, the summations and the superscripts in (22) and (23) can be conveniently dropped without loss of generality.

Taking  $N_{elem}$  as the total number of elements in the discretized geometry,  $\mathbf{d}$  as the unrestrained nodal DOFs, and substituting (22) and (23) into the equations (16) to (20) with correct assembly of the element matrices and imposing boundary conditions, one obtains,

$$(\Lambda^2 \mathbf{M} + \mathbf{K} - P\mathbf{C} + P\mathbf{N}) \mathbf{d} = \mathbf{0} \quad (24)$$

The system mass ( $\mathbf{M}$ ) and stiffness ( $\mathbf{K}, \mathbf{C}, \mathbf{N}$ ) matrices are obtained by evaluating the integrals analytically using commercial symbolic algebra software *Maple*. It can be shown that  $\mathbf{M}$ ,  $\mathbf{K}$  and  $\mathbf{C}$  will yield symmetric matrices while  $\mathbf{N}$  will be non-symmetric matrix. Further, it can be found that the matrices  $\mathbf{M}$ ,  $\mathbf{C}$  and  $\mathbf{N}$  are independent of the circumferential wave number  $n$  while  $\mathbf{K}$  is not. From (24), the eigenvalue problem can be written as,

$$\det(\Lambda^2 \mathbf{M} + \mathbf{K} + P\mathbf{Q}) = 0 \quad (25)$$

where,

$$\mathbf{Q} = \mathbf{N} - \mathbf{C} \quad (26)$$

Damping has been introduced in the structure as mass and stiffness proportional damping (Jung and Han 2014). Identical damping ratios are assumed for the first two vibration modes and the damping matrix can be given as,

$$\mathbf{C} = \gamma_1 \mathbf{M} + \gamma_2 \mathbf{K} \quad (27)$$

where,  $\gamma_1$  and  $\gamma_2$  can be obtained as follows (Chopra 2012),

$$\begin{bmatrix} \gamma_1 \\ \gamma_2 \end{bmatrix} = \begin{bmatrix} \frac{1}{2\Omega_1} & \frac{\Omega_1}{2} \\ \frac{1}{2\Omega_2} & \frac{\Omega_2}{2} \end{bmatrix}^{-1} \begin{bmatrix} \zeta \\ \zeta \end{bmatrix} \quad (28)$$

$\Omega_1$  and  $\Omega_2$  are the first two natural frequencies of the undamped system; the symbol  $\zeta$  is the damping ratio. Incorporating the effect of damping, equation (24) gets modified as,

$$(\Lambda^2 \mathbf{M} + \Lambda \mathbf{C} + \mathbf{K} + P\mathbf{Q})\mathbf{d} = \mathbf{0} \quad (29)$$

The above equation can be transformed into standard linear eigenvalue problem as follows (Langthjem and Sugiyama 2000),

$$\left( \begin{bmatrix} \mathbf{0} & \mathbf{I} \\ -P\mathbf{Q} - \mathbf{K} & -\mathbf{C} \end{bmatrix} - \Lambda \begin{bmatrix} \mathbf{I} & \mathbf{0} \\ \mathbf{0} & \mathbf{M} \end{bmatrix} \right) \begin{bmatrix} \mathbf{d} \\ \Lambda \mathbf{d} \end{bmatrix} = \mathbf{0} \quad (30)$$

$$\mathbf{A}\mathbf{q} = \Lambda \mathbf{q} \quad (31)$$

in which,

$$\mathbf{A} = \begin{bmatrix} \mathbf{0} & \mathbf{I} \\ -\mathbf{M}^{-1}(P\mathbf{Q} + \mathbf{K}) & -\mathbf{M}^{-1}\mathbf{C} \end{bmatrix} \quad (32)$$

$$\mathbf{q} = \begin{bmatrix} \mathbf{d} \\ \Lambda \mathbf{d} \end{bmatrix} \quad (33)$$

The eigenvalues are determined as,

$$\det(\mathbf{A} - \Lambda \mathbf{I}) = 0 \quad (34)$$

In the foregoing discussion,  $\mathbf{0}$  represents a null matrix or vector while  $\mathbf{I}$  represents an identity matrix of appropriate dimension. The eigenvalues  $\Lambda$  can be written as,

$$\Lambda = \Theta \pm i\Omega \text{ with } \Omega \geq 0 \quad (35)$$

Depending upon the values of  $\Theta$  and  $\Omega$ , four distinct cases may arise, as given in *Table 1*.

<b>Table 1</b> Classification of the eigenvalue solution	
Harmonic motion with constant amplitude	$\Theta = 0, \Omega > 0$
Harmonic motion with decreasing amplitude (Damped vibration)	$\Theta < 0, \Omega > 0$
Harmonic motion with increasing amplitude (Flutter instability)	$\Theta > 0, \Omega > 0$
Divergence instability	$\Theta > 0, \Omega = 0$

In the absence of damping and follower force, free vibration of the system is characterized with harmonic motion of constant amplitude, depending on the initial conditions. In case of damped system, the free vibration response is harmonic with decreasing amplitude. With the addition of follower force, the system undergoes flutter or divergence type of instability for

certain critical value of the force depending upon the nature of the eigenvalue. The cyclic frequency ( $f$ ) of the system can be expressed as,

$$f = \frac{\Omega}{2\pi} \quad (36)$$

The eigenvalue problems in (25) and (34) can be written in non-dimensional form by introducing the following parameters,

$$\rho_r = \frac{\rho_i}{\rho_o} \quad (37)$$

$$E_r = \frac{E_i}{E_o} \quad (38)$$

$$\xi_1 = \frac{h}{r_2} \quad (39)$$

$$\xi_2 = \frac{l \sin \alpha}{r_2} \quad (40)$$

$$\lambda = \Lambda r_2 \sqrt{\frac{(1-\nu^2) \rho_o}{E_o}} \quad (41)$$

$$\beta = P \frac{(1-\nu^2)}{E_o h} \quad (42)$$

in which,

$$\lambda = \mathcal{G} \pm i\omega \text{ with } \omega \geq 0 \quad (43)$$

The lowest magnitude of the follower force, for which an instability occurs is the critical load ( $P_{cr}$ ). The non-dimensional critical load is denoted as  $\beta_{cr}$ . A numerical scheme is implemented based on the work of Barsoum (1971) to adaptively increment the load parameter  $\beta$  for determining the onset of instability and the respective non-dimensional critical load for flutter instability.

### 3. Numerical Illustration

The instability characteristics and critical load for flutter are presented in this section by adopting representative values of the pertinent parameters for the conical shell geometry, as adopted in aerospace applications. The presentation is made using the following sub-sections.

#### 3.1. Convergence Study

A computer program is developed using the *MATLAB* platform for the finite element analysis of free vibration and dynamic instability of truncated shell geometry subjected to follower

force. Only the mass, and elastic stiffness matrices are retained in the free vibration eigen analysis presented in equation (25).

The boundary conditions are denoted by  $F$ ,  $S$ , and  $C$  for the free, simply supported and clamped cases, respectively, at each end of the shell. The subscripts  $S$  and  $L$  refers to the smaller and larger ends of the shell, respectively. The constituent material properties for the FGM are adopted from Tornabene et al. (2009) and Zhao and Liew (2011), as furnished in *Table 2*. The value of the Poisson's ratio is assumed to be constant as 0.3.

<b>Table 2</b> Properties of the individual homogeneous constituents			
<b>Material</b>	<b>Poisson's ratio</b>	<b>Young's modulus</b>	<b>Density</b>
Metal (Aluminum)	0.3	70 GPa	2707 kg/m <sup>3</sup>
Ceramic – 1 (Zirconia)	0.3	151 GPa	3000 kg/m <sup>3</sup>
Ceramic – 2	0.3	168 GPa	5700 kg/m <sup>3</sup>

A convergence study is performed to determine the number of finite elements required to suitably represent the cases of homogeneous and FGM shells for different parameter values. For this, the undamped natural frequencies of the first few modes are determined considering varying finite element discretization of the shell geometry. The convergence plots of the five lowest non-dimensional frequencies are given in *Figure 4* for a homogeneous shell for two boundary conditions ( $S_S - S_L$  and  $S_S - C_L$ ) using the PFGM model with  $\eta \rightarrow \infty$  assuming any constituent material.

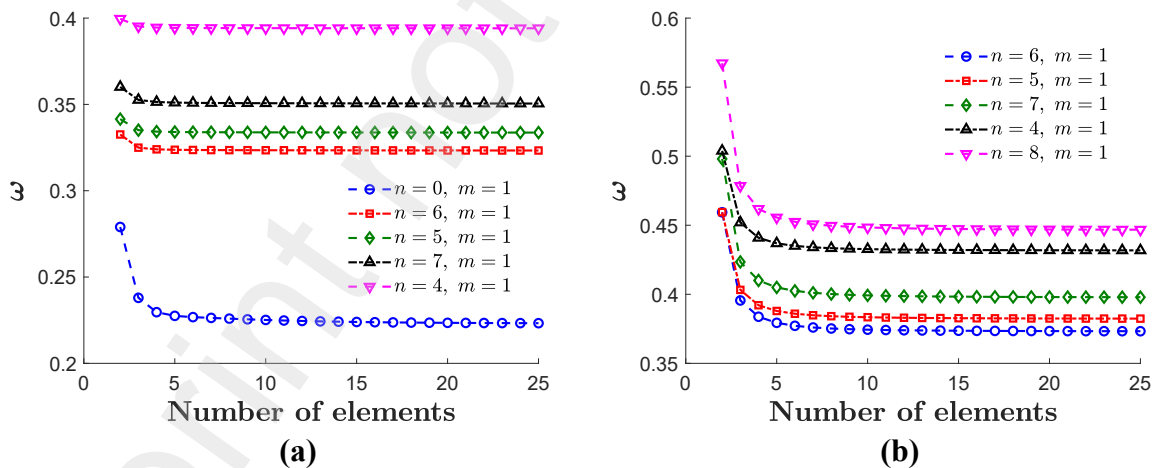


**Figure 4** Convergence of  $\omega$  with PFGM,  $\eta \rightarrow \infty$ ,  $\alpha = 45^\circ$ ,  $\xi_1 = 0.01$ ,  $\xi_2 = 0.5$ ,  $\zeta = 0$   
(a)  $S_S - S_L$  (b)  $S_S - C_L$

Similarly, the convergence plots for the five lowest cyclic frequencies are also shown in *Figure 5* for two volume fraction indices of a PFGM truncated conical shell with aluminum as the outer constituent and ceramic – 2 as the inner constituent materials.

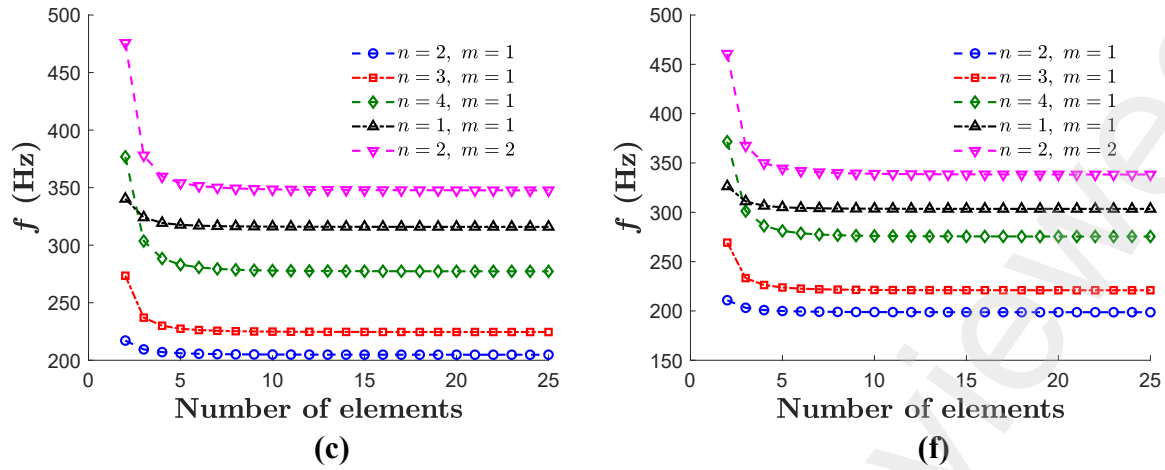


**Figure 5** Convergence of  $f$  (Hz) with  $F_S-C_L$ , PFGM,  $\alpha = 40^\circ$ ,  $\xi_1 = 0.0459$ ,  $\xi_2 = 0.7705$ ,  $\zeta = 0$ ,  $r_2 = 2.178$  m (a)  $\eta = 1$  (b)  $\eta = 50$

The cases with  $\eta \rightarrow \infty$  are numerically mimicked by adopting a large value of  $10^{30}$ . The convergence results are presented in *Table 3* and *Table 4*. The values in the brackets represent the corresponding circumferential and longitudinal mode numbers  $(n, m)$ .

<b>Table 3</b> Convergence of lowest non-dimensional undamped natural frequency ( $\omega$ ) of truncated conical shell with homogeneous material properties $\alpha = 45^\circ$ , $\xi_1 = 0.01$ , $\xi_2 = 0.5$					
Support	Number of elements ( $N_{elem}$ )				
	5	10	15	20	25
$S_S-S_L$	0.2275 (0,1)	0.2251 (0,1)	0.2240 (0,1)	0.2235 (0,1)	0.2233 (0,1)
$S_S-C_L$	0.3793 (6,1)	0.3744 (6,1)	0.3736 (6,1)	0.3734 (6,1)	0.3733 (6,1)

The natural frequencies are observed to converge well for around 15 elements for both the homogeneous as well as FGM shells. Henceforth, both the free vibration and dynamic instability analyses employ 20 elements to reasonably discretize the shell along its slanted length.

<b>Table 4</b> Convergence of lowest undamped natural frequency ( $f$ in Hz) of truncated conical shell with PFGM model, $F_S-C_L$ boundary, $E_i = 168$ GPa, $\rho_i = 5700$ kg/m <sup>3</sup> , $E_o = 70$ GPa, $\rho_o = 2707$ kg/m <sup>3</sup> , $\alpha = 40^\circ$ , $\xi_1 = 0.0459$ , $\xi_2 = 0.7705$ , $r_2 = 2.178$ m					
$\eta$	Number of elements ( $N_{elem}$ )				
	5	10	15	20	25
1	206.09 (2,1)	204.99 (2,1)	204.85 (2,1)	204.81 (2,1)	204.80 (2,1)
50	199.92 (2,1)	198.86 (2,1)	198.74 (2,1)	198.70 (2,1)	198.69 (2,1)

### 3.2. Verification of Results

The results from the free vibration analyses are verified against the ones reported in literature for the homogeneous and the PFGM truncated conical shells. The non-dimensional

undamped free vibration frequencies of the first longitudinal mode ( $m = 1$ ) for homogeneous truncated conical shell are obtained from the PFGM model by adopting  $\eta \rightarrow \infty$  with any of the constituent materials. The results are compared with Irie et al. (1984), Shu (1996) and Liew et al. (2005) (for different boundary conditions) in *Table 5*. For higher circumferential modes, the frequencies obtained from the present analysis are lower than that from the literature due to inclusion of the effect of rotary inertia.

<b>Table 5</b> Non-dimensional undamped natural frequency ( $\omega$ ) of truncated conical shell with homogeneous material, $\alpha = 45^\circ$ , $\xi_1 = 0.01$ , $\xi_2 = 0.5$ , $m = 1$ , $N_{elem} = 20$								
	Present	Irie et al. (1984)	Shu (1996)	Liew et al. (2005)	Present	Irie et al. (1984)	Shu (1996)	Liew et al. (2005)
$n$	$S_S-S_L$				$S_S-C_L$			
0	0.2235	0.2233	0.2233	0.2234	0.8699	0.8698	0.8700	0.8691
1	0.5462	0.5462	0.5463	0.5462	0.8117	0.8117	0.8118	0.8113
2	0.6309	0.6310	0.6310	0.6309	0.6613	0.6614	0.6613	0.6610
3	0.5062	0.5065	0.5062	0.5061	0.5247	0.5249	0.5246	0.5244
4	0.3941	0.3947	0.3942	0.3941	0.4319	0.4324	0.4319	0.4316
5	0.3337	0.3348	0.3340	0.3337	0.3825	0.3834	0.3826	0.3822
6	0.3233	0.3248	0.3239	0.3235	0.3734	0.3747	0.3737	0.3732
7	0.3505	0.3524	0.3514	0.3510	0.3980	0.3997	0.3987	0.3980
8	0.4012	0.4033	0.4023	0.4019	0.4469	0.4489	0.4479	0.4472
9	0.4660	0.4684	0.4676	0.4671	0.5120	0.5142	0.5133	0.5124

The  $C_S-F_L$  boundary condition is used in this work to determine the free vibration and stability characteristics under follower force. The non-dimensional natural frequencies with  $C_S-F_L$  boundary conditions for different  $\alpha$  and  $\xi_2$  values are presented and compared with Irie et al. (1984) in *Table 6* for homogeneous material.

<b>Table 6</b> Non-dimensional undamped natural frequency ( $\omega$ ) of truncated conical shell with homogeneous material, $C_S-F_L$ boundary, $\xi_1 = 0.01$ , $m = 1$ , $N_{elem} = 20$						
	Present	Irie et al. (1984)	Present	Irie et al. (1984)	Present	Irie et al. (1984)
$n$	$\xi_2 = 0.25, \alpha = 30^\circ$		$\xi_2 = 0.25, \alpha = 45^\circ$		$\xi_2 = 0.25, \alpha = 60^\circ$	
0	0.8311	0.8312	0.6857	0.6859	0.4965	0.4966
1	0.6767	0.6768	0.6220	0.6221	0.4671	0.4672
2	0.4831	0.4831	0.5038	0.5039	0.4057	0.4059
3	0.3551	0.3553	0.4040	0.4042	0.3477	0.3480
$n$	$\xi_2 = 0.75, \alpha = 30^\circ$		$\xi_2 = 0.75, \alpha = 45^\circ$		$\xi_2 = 0.75, \alpha = 60^\circ$	
0	0.2267	0.2266	0.3205	0.3205	0.3926	0.3926
1	0.1187	0.1182	0.1576	0.1574	0.1502	0.1500
2	0.0549	0.0549	0.0780	0.0779	0.0772	0.0771
3	0.0458	0.0469	0.0573	0.0579	0.0590	0.0593

The first five natural frequencies for PFGM truncated conical shell with aluminum as outer constituent and ceramic – 2 as inner constituent are determined for different values of  $\eta$  with  $F_S-C_L$  support condition. These are shown in *Table 7* and compared with the results reported by Tornabene et al. (2009). The values in brackets respectively denote the circumferential and longitudinal mode numbers.

<b>Table 7</b> Undamped cyclic natural frequency ( $f$ in Hz) of truncated conical shell with PFGM model, $F_S-C_L$ boundary, $E_i = 168$ GPa, $\rho_i = 5700$ kg/m <sup>3</sup> , $E_o = 70$ GPa, $\rho_o = 2707$ kg/m <sup>3</sup> , $\alpha = 40^\circ$ , $\xi_1 = 0.0459$ , $\xi_2 = 0.7705$ , $r_2 = 2.178$ m, $N_{elem} = 20$				
	Present	Tornabene et al. (2009)	Present	Tornabene et al. (2009)
<b><math>f</math> (Hz)</b>	<b><math>\eta = 0</math> (Ceramic)</b>		<b><math>\eta = 0.6</math></b>	
1	210.03 (2,1)	209.99	205.88 (2,1)	205.96
2	232.09 (3,1)	231.96	225.63 (3,1)	225.52
3	288.09 (4,1)	287.48	278.52 (4,1)	277.93
4	322.67 (1,1)	322.57	317.89 (1,1)	318.18
5	357.28 (2,2)	356.95	349.57 (2,2)	349.48
<b><math>f</math> (Hz)</b>	<b><math>\eta = 1</math></b>		<b><math>\eta = 5</math></b>	
1	204.81 (2,1)	204.91	203.84 (2,1)	203.93
2	224.56 (3,1)	224.44	227.86 (3,1)	227.67
3	277.29 (4,1)	276.66	285.02 (4,1)	284.26
4	315.93 (1,1)	316.32	309.19 (1,1)	309.57
5	347.72 (2,2)	347.66	347.21 (2,2)	347.08
<b><math>f</math> (Hz)</b>	<b><math>\eta = 20</math></b>		<b><math>\eta = 50</math></b>	
1	200.72 (2,1)	200.79	198.70 (2,1)	198.73
2	224.39 (3,1)	224.29	220.97 (3,1)	220.86
3	280.71 (4,1)	280.15	275.47 (4,1)	274.93
4	304.93 (1,1)	305.04	303.46 (1,1)	303.46
5	342.02 (2,2)	341.87	338.32 (2,2)	338.11
<b><math>f</math> (Hz)</b>	<b><math>\eta = 100</math></b>		<b><math>\eta \rightarrow \infty</math> (Metal)</b>	
1	197.80 (2,1)	197.79	196.73 (2,1)	196.69
2	219.34 (3,1)	219.21	217.39 (3,1)	217.23
3	272.92 (4,1)	272.38	269.85 (4,1)	269.28
4	302.87 (1,1)	302.83	302.24 (1,1)	302.14
5	336.64 (2,2)	336.39	334.65 (2,2)	334.35

It can be seen from *Table 7* that the frequencies in a particular mode are highest when a shell is composed entirely of ceramic material ( $\eta = 0$ ) and becomes lowest for a homogeneous shell made up of aluminum ( $\eta \rightarrow \infty$ ). This is because the effect of an increase in Young's modulus on the frequency in a ceramic shell is more pronounced than the effect of increased density when compared with the metallic shell, i.e.,  $E_r > \rho_r$ .



The results in *Table 5*, *Table 6* and *Table 7* show that the natural frequencies obtained from the present analysis for homogeneous or FGM truncated conical shells are in good agreement with the ones in existing literature.

### 3.3. Free Vibration Characteristics

The free vibration characteristics of the truncated conical shells are briefly reviewed in this section with special emphasis on the natural frequencies. This is because these modes have important bearing or participation in dynamic instabilities in the form of flutter.

Free vibration characteristics of the PFGM model with zirconia on the inner surface and aluminum on the outer surface of the truncated conical shell with  $C_S-F_L$  boundary conditions are presented herein. The natural frequencies are only presented. *Figure 6* presents the variations in the non-dimensional natural frequencies with varying semi-vertex angle ( $\alpha$ ) for the first four circumferential modes with two damping ratios ( $\zeta = 0, 0.2$ ) for only the first longitudinal mode ( $m = 1$ ). The curves for intermediate damping ratios lie between these two curves. It can be seen that the damped natural frequencies do not vary significantly from the undamped frequencies even at 20 percent damping, which, of course is an unrealistically large value of damping for FGM in practical cases. Further, it is also found that for lower  $\alpha$  the disparity between the damped and undamped frequencies is even smaller as compared to that at large  $\alpha$ .

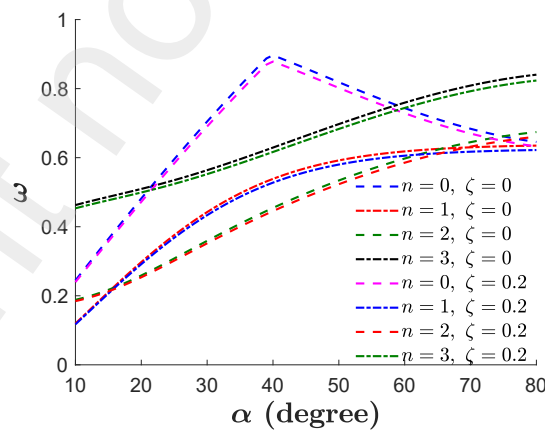


**Figure 6** Variation of  $\omega$  with  $\alpha$  for  $C_S-F_L$ , PFGM,  $\eta = 1$ ,  $\xi_1 = 0.15$ ,  $\xi_2 = 0.5$ ,  $m = 1$

The variation of the first non-dimensional longitudinal frequency with different circumferential modes shows bath tub shapes in *Figure 7*. The natural frequencies decrease for increasing values of  $\eta$  with the chosen constituents due to the reason discussed in the preceding section, i.e.,  $E_r > \rho_r$ . The lowest frequencies occur at  $n = 1, 2, 2, 1$  (circumferential

modes) for  $\alpha = 10^\circ, 30^\circ, 60^\circ, 80^\circ$  respectively. It is also interesting to note that the circumferential mode corresponding to the lowest frequency does not change with change in the  $\eta$  values. The mode shapes corresponding to the circumferential modes  $n = 0$  (first) and  $n = 1$  (second) are referred as the ‘breathing’ and ‘flexural’ modes, respectively.

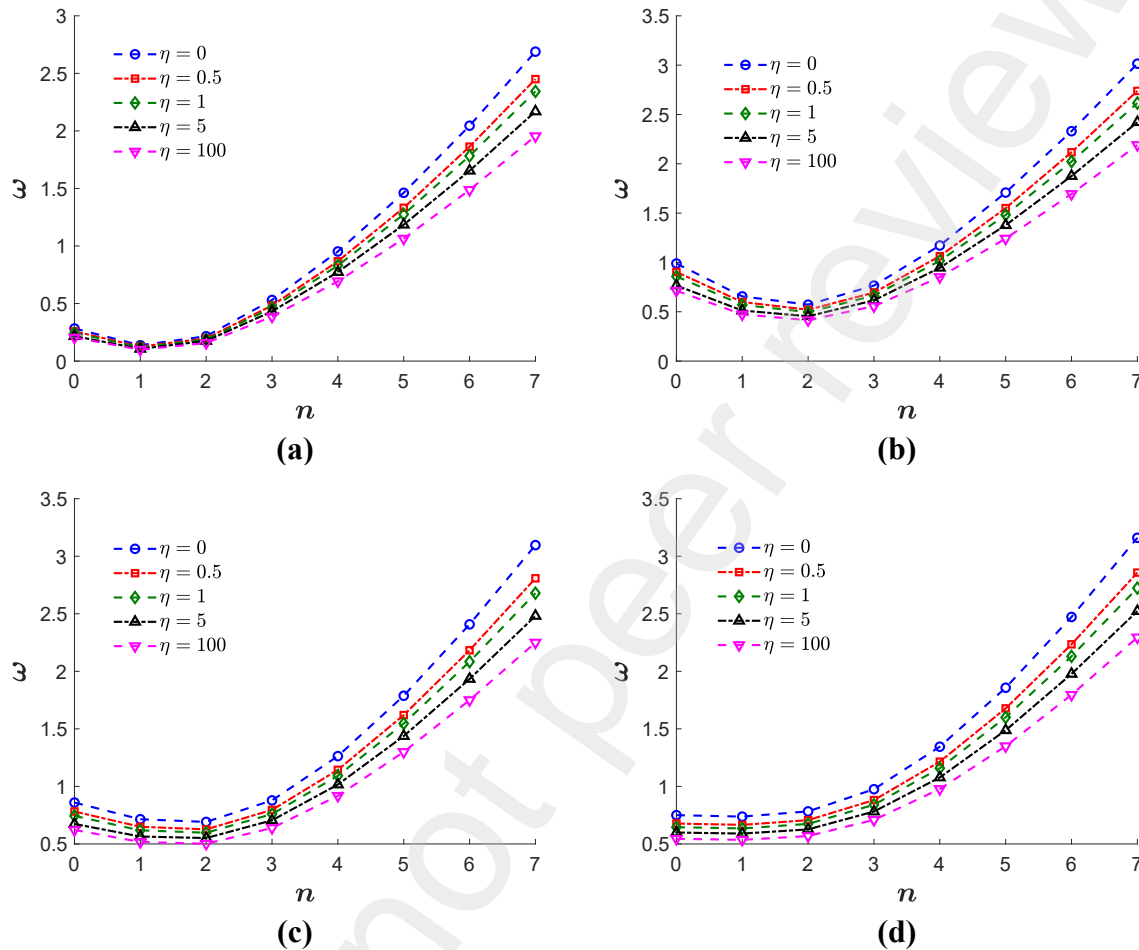


**Figure 7** Variation of  $\omega$  with  $n$  for  $C_S$ - $F_L$ , PFGM,  $\xi_1 = 0.15$ ,  $\xi_2 = 0.5$ ,  $\zeta = 0$ ,  $m = 1$   
 (a)  $\alpha = 10^\circ$  (b)  $\alpha = 30^\circ$  (c)  $\alpha = 60^\circ$  (d)  $\alpha = 80^\circ$

### 3.4. Dynamic Instability Analysis

Non-zero magnitude of the constant follower force is adopted while solving the eigenvalue problem in (25) and (34) in search for flutter instability. The PFGM and EFGM models are considered assuming the outer and inner surfaces to be composed of metallic (aluminum) and ceramic (zirconia) constituents, respectively. Relevant properties were presented in Table 2.

This choice of the constituent materials for the FGM is logical since, in the exit cones of launch vehicles, the inner lining of the conical surface is exposed to very high temperatures from the exhaust of the rocket engines. In such cases, ceramics like zirconia can be effectively used as a heat-resistant material. Additionally, aluminum can be employed as a

lightweight material on the outer surface of the FGM. In order to simulate the boundaries of a rocket nozzle, the smaller end is taken as clamped, where it is typically welded or forged to the body of the launch vehicle. The larger end of the shell is kept free. The thickness-wise variation of the density and Young's modulus in the shell for these two FGMs (with the chosen materials) are shown in *Figure 8* and *Figure 9*. For the PFGM model, the density and Young's modulus at any depth are dependent on the volume fraction index  $\eta$ .

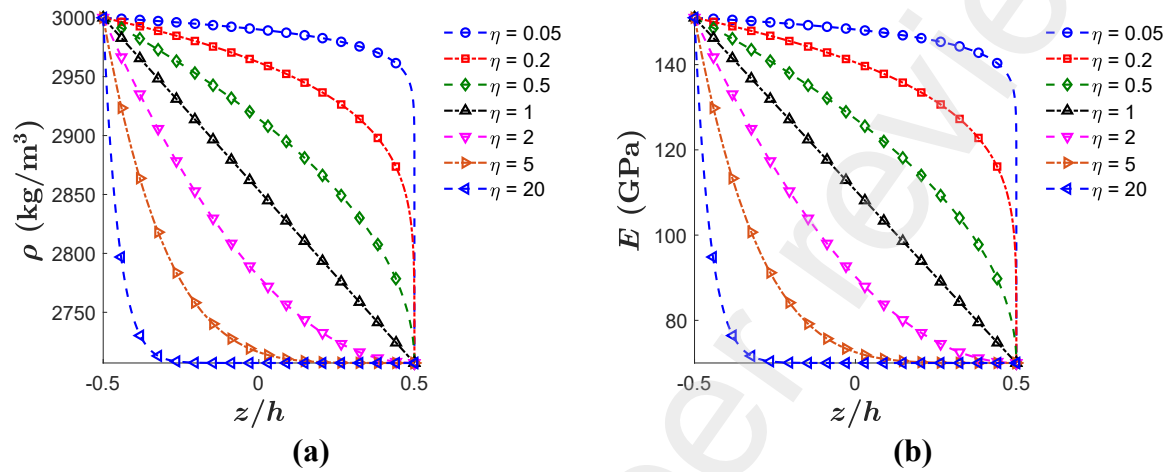


**Figure 8** Variation of material properties across the thickness with varying  $\eta$  for PFGM  
(a)  $\rho$  with  $z/h$  (b)  $E$  with  $z/h$

For EFGM, however, the variation between the two surfaces is almost linear for density, whereas the Young's modulus shows a slight nonlinear variation. The stability behavior of the EFGM model is expected to be identical to that of the PFGM with  $\eta = 1$ .

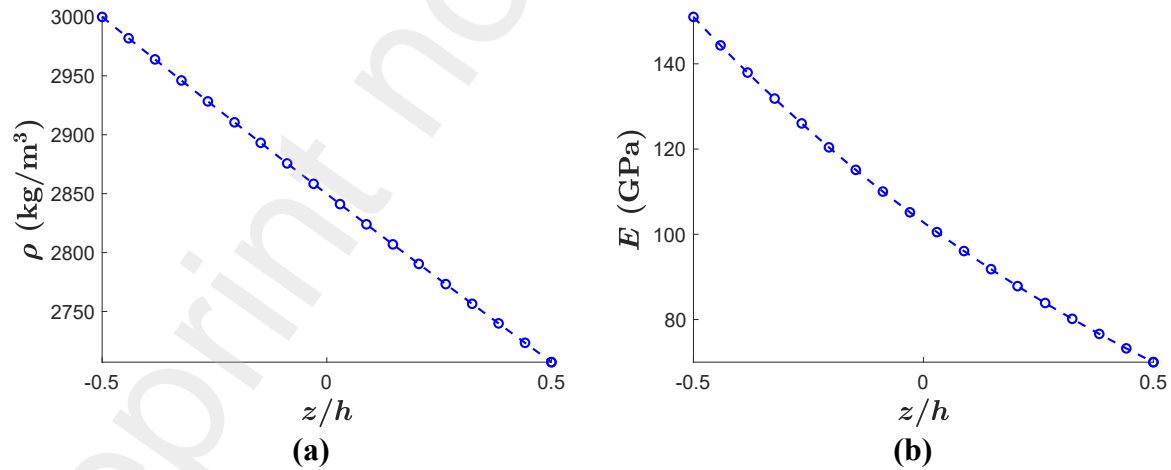


**Figure 9** Variation of material properties across the thickness for the EFGM  
(a)  $\rho$  with  $z/h$  (b)  $E$  with  $z/h$

In determination of the flutter load, up to four circumferential ( $n = 0, 1, 2, 3$ ) and four longitudinal modes ( $m = 1, 2, 3, 4$ ) are considered for the undamped shell. Analysis in higher

modes may require higher-order shear deformation theories, for improved accuracy in the estimation of the displacement fields. All the longitudinal modes ( $m = 1, 2, 3, \dots$ ) and the first four circumferential modes ( $n = 0, 1, 2, 3$ ) are considered for estimating the flutter load in damped shells. In absence of damping, the dynamic instabilities explored by the present analysis are strictly of flutter-type. In this type of instability, two frequencies of the same circumferential mode ( $n$ ) coalesce for certain magnitude of the follower force. Inclusion of the follower force results in non-zero imaginary part of  $\lambda^2$ . Because of this, the shells experience motion with increasing amplitude under the constant follower force with progress in time.

Figure 10 shows the plots of the real (a and b) and imaginary parts (c and d) of the squared non-dimensional frequency parameter subjected to varying non-dimensional load in undamped shell with characteristic geometry and material parameters. The flutter (critical) load can be identified from these plots.

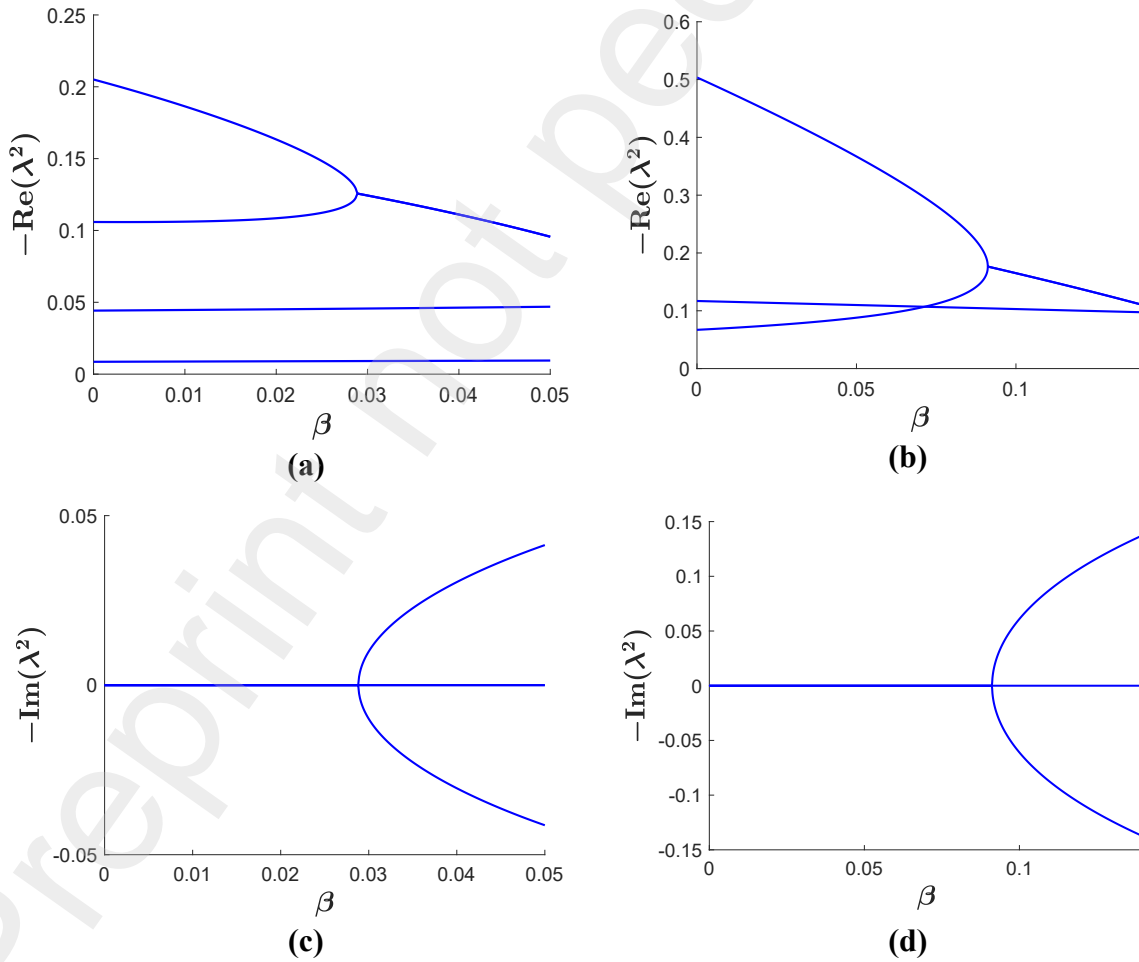


**Figure 10** Flutter instability for PFGM,  $\zeta = 0$ ,  $n = 0$

(a and c)  $\eta = 10$ ,  $\alpha = 30^\circ$ ,  $\xi_1 = 0.1$ ,  $\xi_2 = 0.7$  (b and d)  $\eta = 1$ ,  $\alpha = 50^\circ$ ,  $\xi_1 = 0.15$ ,  $\xi_2 = 0.5$

Figure 10a, shows that the real parts of the third and fourth ( $m = 3, 4$ ) eigenvalues coalesce, accompanied by non-zero values of the imaginary parts. Likewise, Figure 10b shows coalescence of the second and third longitudinal eigenmodes (i.e.  $m = 2, 3$ ). Coalescence of the real-parts of any two modes (accompanied by non-zero imaginary parts) indicates the onset of the flutter. The algorithm implemented herein ensures that the eigenvalues are sorted based on the magnitude of the real part of  $\lambda^2$  for non-zero value of the follower force to determine the corresponding longitudinal ( $m$ ) mode.

Both flutter and divergence type instability have been found for the damped system. For this case, the system eigenvalues are twice in number as compared to the undamped case. The flutter instability is found to be critical for all parameter values because it occurs under a lower magnitude of the follower force. The possible solutions were illustrated in Table 1.

Weak flutter instabilities are observed for certain combination of the pertinent parameter values. The critical follower force value for weak flutter are considerably lower than the general trend of the flutter load in the parameter space. The weak flutter instabilities disappear on increasing follower force magnitude beyond a particular value, unlike strong flutter instability. Subsequent to weak flutter, a strong flutter is again observed at a higher magnitude of follower force, which does not go away with increasing value of the follower force. Instances of weak flutter and subsequent strong flutter are shown in Figure 11a-d considering an undamped shell.

Subplots (a, c) and (b, d) show that the second and third longitudinal modes coalesce first for certain value of the follower force, indicating weak flutter. However, the coalesced eigenpath subsequently bifurcates into two distinct eigenpaths at a higher magnitude of the follower force. On increasing the follower force even higher, the first and second frequencies are shown to coalesce to give rise to a strong flutter instability.

The weak flutter instabilities are significantly suppressed in the presence of damping. At higher damping values, such weak instabilities get suppressed even more, and the plot of the critical load becomes a smooth curve in the parametric space. It can be attributed to the fact that the stability of the structure enhances with increased damping as it helps in the dissipation of energy in the system through alternate path resulting in higher critical loads.

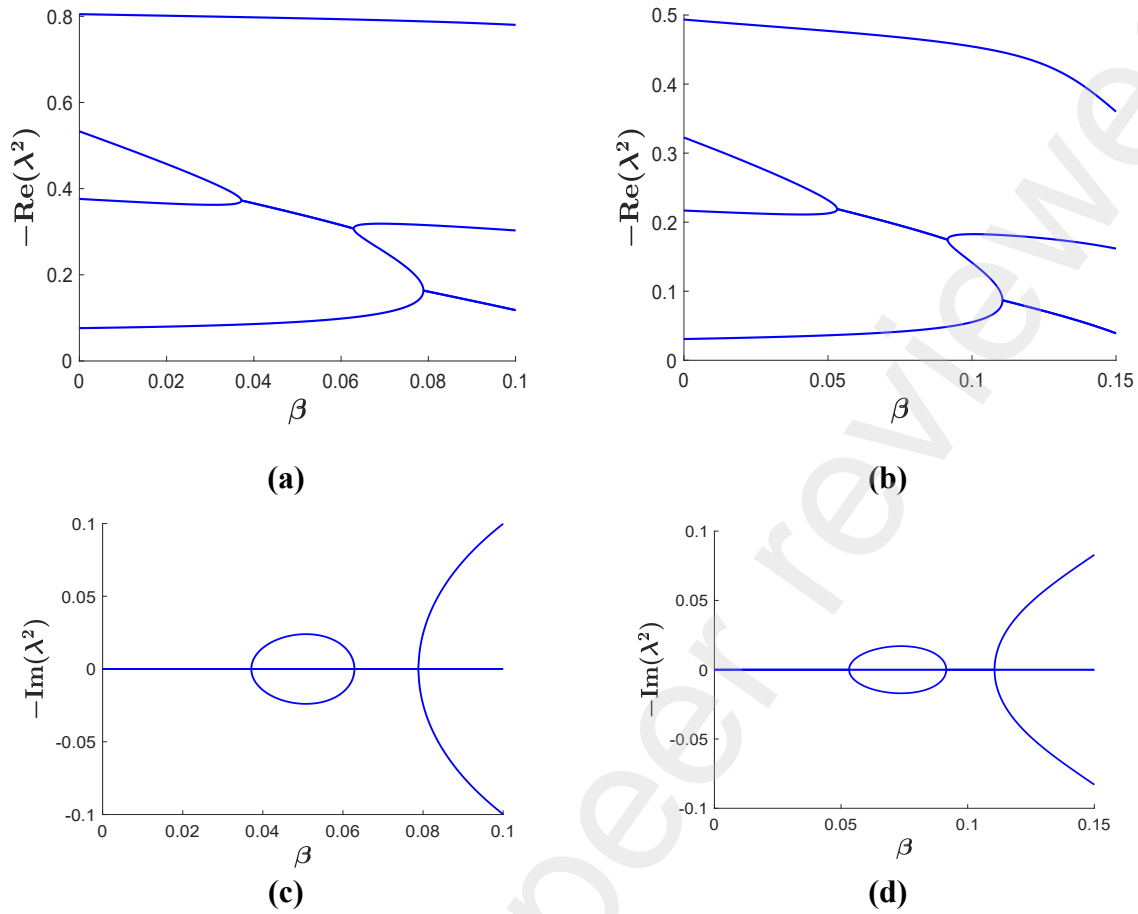


**Figure 11** Strong and weak flutter loads for PFGM,  $\zeta = 0$ ,  $n = 1$

(a and c)  $\eta = 10$ ,  $\alpha = 10^\circ$ ,  $\xi_1 = 0.12$ ,  $\xi_2 = 0.1$  (b and d)  $\eta = 5$ ,  $\alpha = 30^\circ$ ,  $\xi_1 = 0.16$ ,  $\xi_2 = 0.4$

### 3.5. Influence of parametric variations on the flutter load

Parametric variations of the non-dimensional flutter load considering different material and geometric parameters of the truncated conical shell are presented for the power-law and exponential gradations of the FGM.

Parametric variations of the non-dimensional flutter load  $\beta_{cr}$  with varying gradation index  $\eta$  are shown in *Figure 12a-d* for varying  $\xi_2$ ,  $\xi_1$ ,  $\alpha$ ,  $\zeta$  respectively. Common to all these plots is the reducing critical load with increasing metallic constituent, marked by higher gradient index ( $\eta$ ). This trend can be attributed to the fact that the non-dimensional frequencies of the truncated conical shell decrease for higher volume fraction indices, previously demonstrated in *Figure 7a-d*. Maximum critical load is observed for ceramic shells yet functional gradation is desirable to incorporate the lightweight metallic constituent

in the shell. Results are presented hereafter for only two values of  $\eta$  ; namely  $\eta=1$  and  $\eta=5$  . The former ( $\eta=1$ ) gives a linear variation of the volume fraction in the FGM.

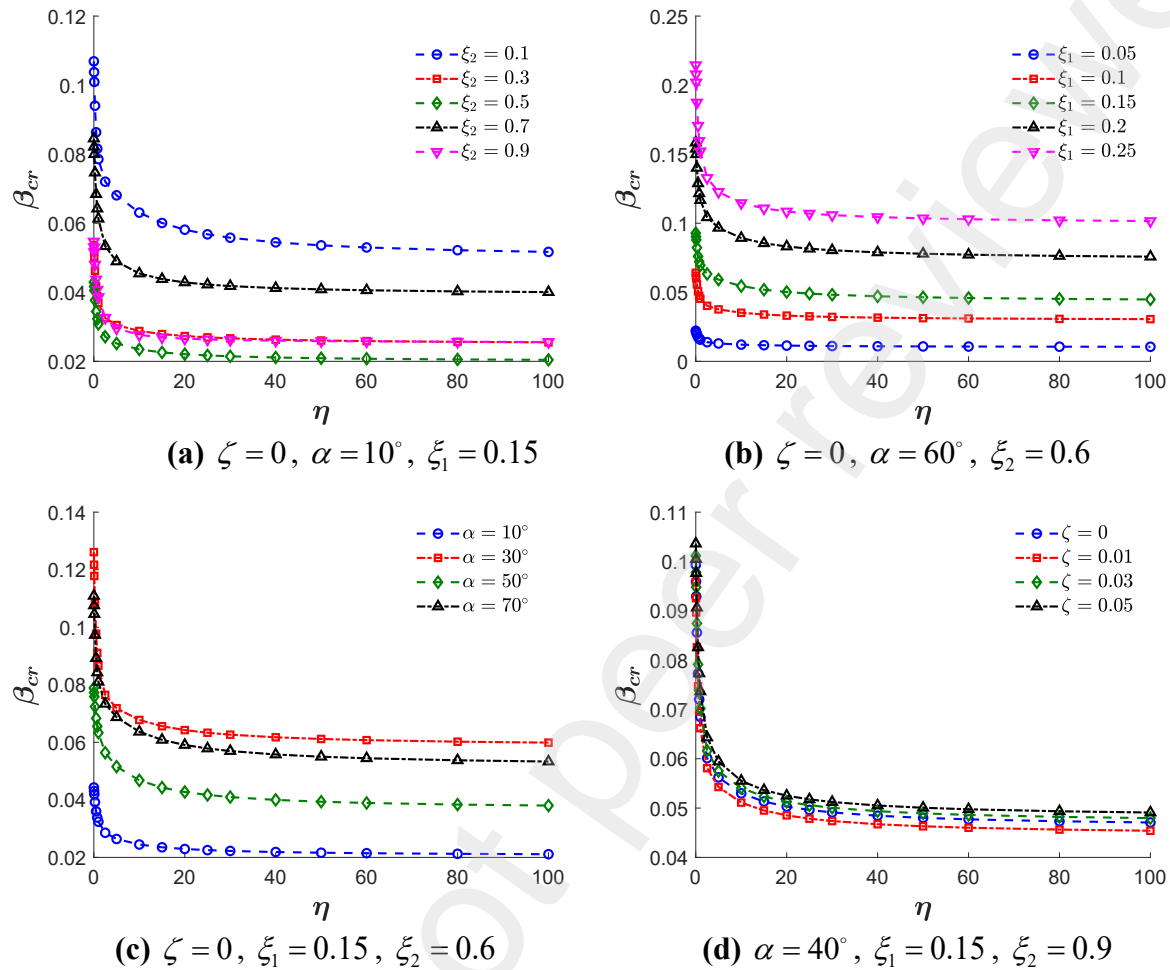


**Figure 12** Variation of  $\beta_{cr}$  with  $\eta$  for PFGM with varying (a) slenderness parameter ( $\xi_2$ ) (b) thickness parameter ( $\xi_1$ ) (c) semi-vertex angle ( $\alpha$ ) (d) damping ratio ( $\zeta$ )

Figure 13 presents the variations in the non-dimensional critical load for varying value of the thickness parameter ( $\xi_1$ ). The trends are presented for varying level of damping ( $\zeta = 0, 0.01, 0.03, 0.05$ ). The subplots (a-d) considers varying combination of ( $\eta, \xi_2, \alpha$ ), listed therein. The critical load increases with higher damping ratios. However, the increase in the critical load beyond around three percent damping is negligible in most cases. As discussed previously, the sudden drops in the load parameter for low  $\zeta$  values are due to the formation of weak flutter instabilities, which of course stabilizes for increased values of damping.

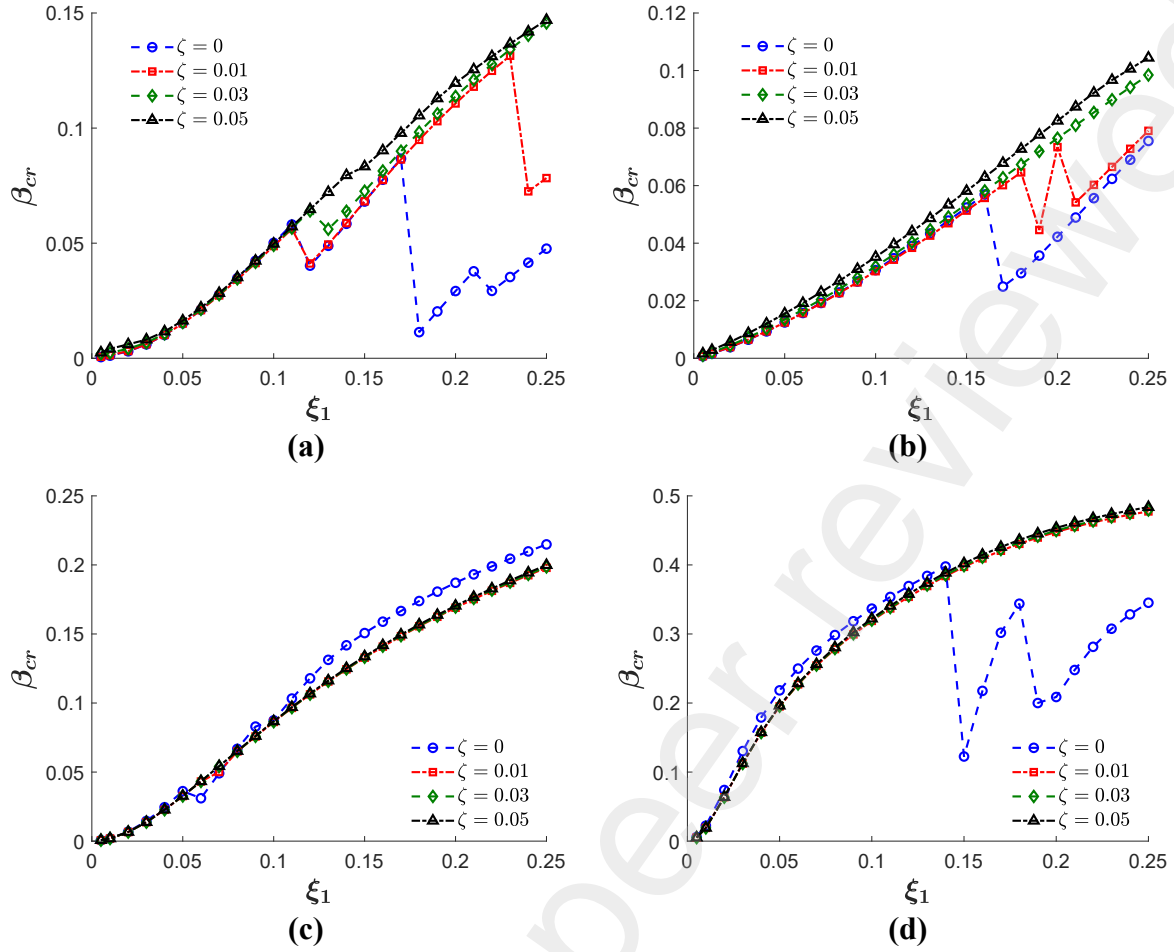


**Figure 13** Variation of  $\beta_{cr}$  with  $\xi_1$  for varying  $\zeta$  for PFGM (a)  $\eta = 5$ ,  $\xi_2 = 0.1$ ,  $\alpha = 10^\circ$  (b)  $\eta = 5$ ,  $\xi_2 = 0.7$ ,  $\alpha = 30^\circ$  (c)  $\eta = 5$ ,  $\xi_2 = 0.3$ ,  $\alpha = 60^\circ$  (d)  $\eta = 1$ ,  $\xi_2 = 0.1$ ,  $\alpha = 80^\circ$

The curve for  $\zeta = 0$  should ideally always be below the other  $\zeta$  curves, but this is not observed for certain instances. Such anomalous behavior can be attributed to the fact that the present analysis includes only four initial longitudinal modes for the undamped case. Many more weak instabilities could be found, if higher longitudinal modes are included in the analysis. This would have caused the  $\zeta = 0$  curve to always lie below the higher  $\zeta$  curves. Subsequent results presented herein are shown by taking only zero and three percent damping in the first two modes, which is reasonable for all practical purposes.

The critical load corresponding to the identical circumferential wave numbers and identical coalescing longitudinal modes follows a smooth curve, as presented in *Figure 14a-b*. The isolated points indicate that they are not part of any of the plotted eigenmodes. The critical load curve in the parametric space (denoted by a solid line) is obtained by joining the lowest non-dimensional loads corresponding to each parameter value.



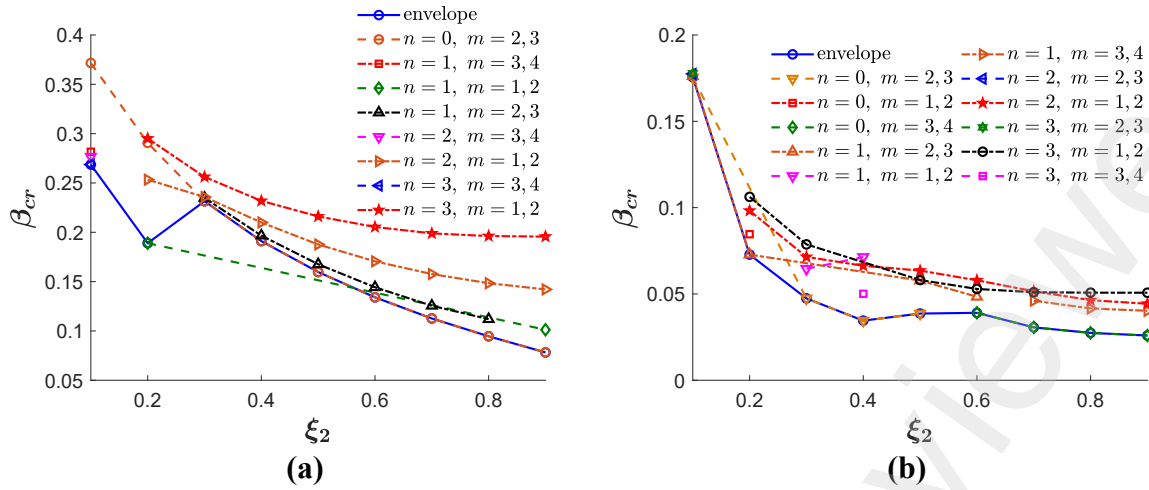


**Figure 14** Variation of  $\beta_{cr}$  with  $\xi_2$  for identical eigenmodes for PFGM,  $\eta = 5$ ,  $\zeta = 0$   
**(a)**  $\alpha = 80^\circ$ ,  $\xi_1 = 0.25$  **(b)**  $\alpha = 30^\circ$ ,  $\xi_1 = 0.1$

The plots of the non-dimensional critical load ( $\beta_{cr}$ ) with varying thickness parameter ( $\xi_1$ ) are presented in *Figure 15* to *Figure 17* for different values of the length parameters ( $\xi_2$ ), damping ratio ( $\zeta$ ), semi-vertex angle ( $\alpha$ ) and volume fraction index ( $\eta$ ) for the PFGM. In *Figure 15b*, the number of drops in critical load due to weak instabilities reduces as compared to *Figure 15a* due to increased damping. *Figure 15* and *Figure 16* show that the weak instabilities tend to lie in identical regions on the parametric space for different  $\eta$ . An increasing trend in the critical load with increasing thickness parameter ( $\xi_1$ ) is seen, which is evident as thicker shells should exhibit instability under larger follower force, if other parameters remain identical. Critical loads are lower for shells with higher values of length parameter ( $\xi_2$ ) for any range of the semi-vertex angle. Increased  $\xi_2$  keeping other parameters constant implies that the shell is longer and hence becomes more susceptible to instability. Moreover, weak instabilities are not that frequent for shells having large  $\xi_2$  values. This is because such shells being longer are comparatively more unstable. Hence the onset of any instability is expected to grow and dominate as strong flutter instability in the system. Keeping other parameters constant, the critical load also increases with increasing semi-vertex angle of the conical shell.

Roughly in the range of  $0.7 \leq \xi_2 \leq 0.9$  and  $\alpha \leq 40^\circ$ , the critical load parameter ( $\beta_{cr}$ ) attains saturation or varies negligibly beyond a certain  $\xi_1$ . Although  $\beta_{cr}$  remains constant, it does not imply that the dimensional critical load will also be constant. This is because the dimensional load is proportional to the thickness of the shell, and it increases linearly due to

increasing  $\xi_1$ . Interestingly, a similar observation has also been reported in the case of a completely free cylindrical shell subjected to follower force by Park and Kim (2000).

It follows from the present study that such a phenomenon of the constant non-dimensional critical load must also exist in the case of sufficiently long cylindrical shells under follower force with  $C_S-F_L$  boundary conditions (Torki et al. 2014b). It is because a truncated conical shell with small  $\alpha$  and large  $\xi_2$  values can be approximated as a long cylindrical shell in the limiting sense. In general, the non-dimensional critical load of the truncated conical shell reduces for a decrease in the semi-vertex angle, reduction in thickness, or an increase in the length of the shell.

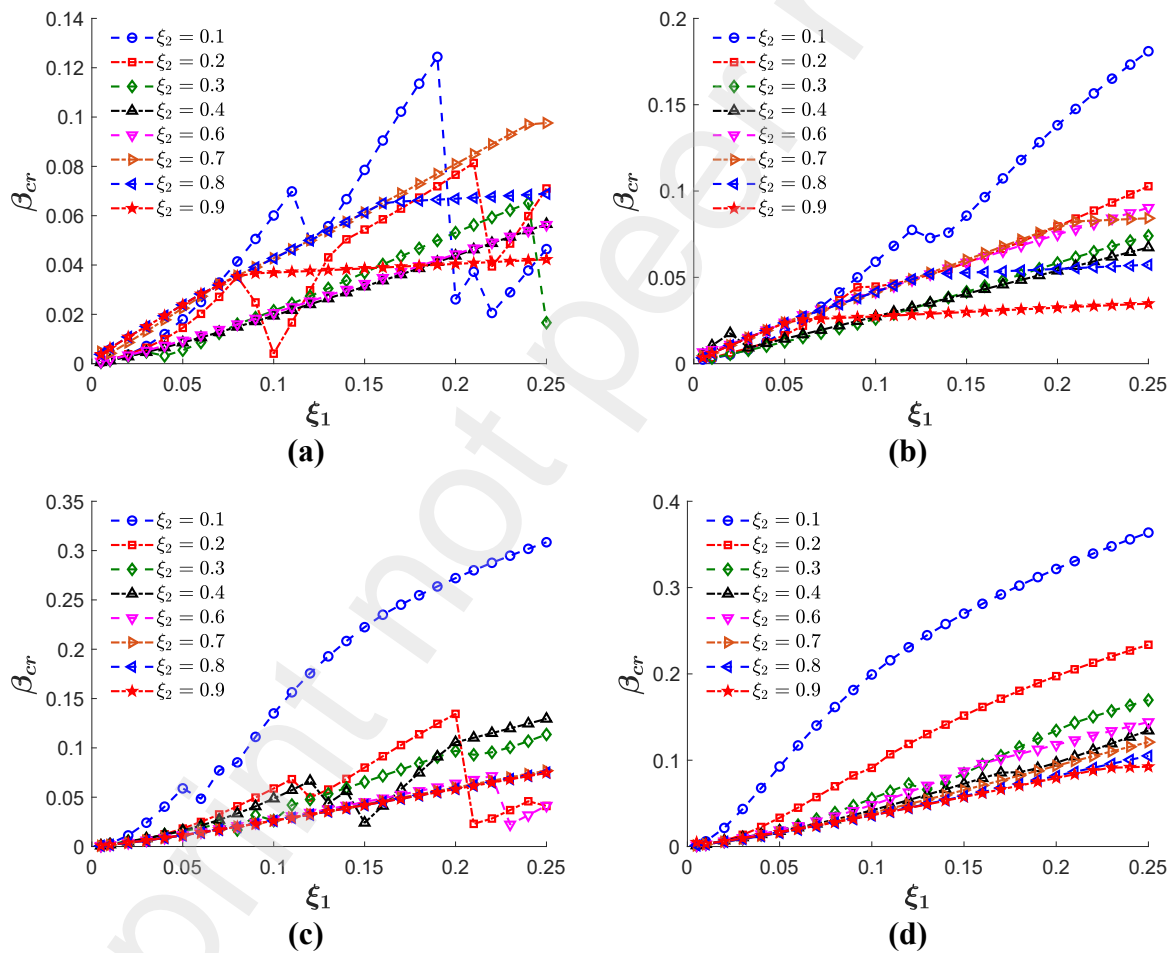
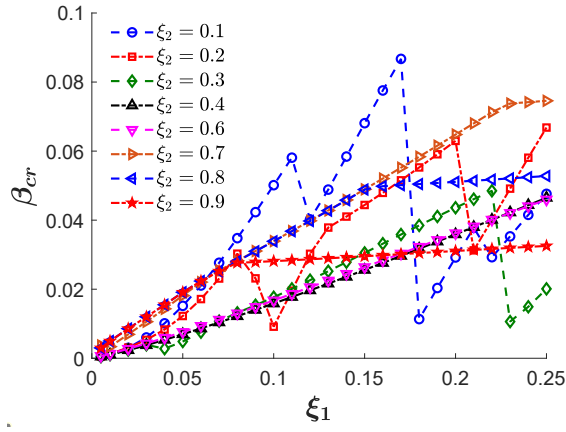
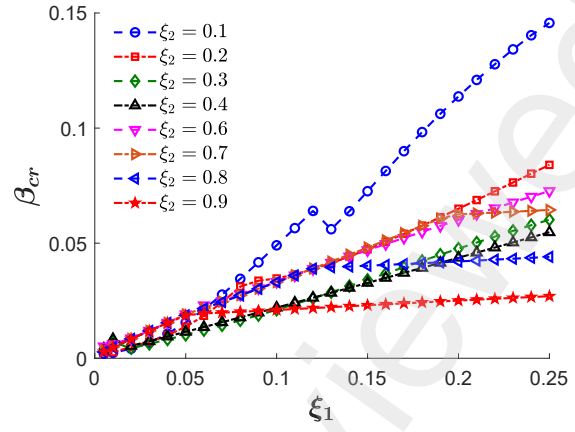


**Figure 15** Variation of  $\beta_{cr}$  with  $\xi_1$  for varying  $\xi_2$  for PFGM,  $\eta = 1$

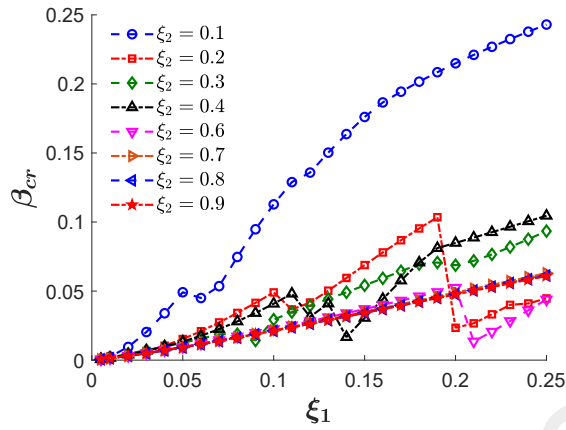
(a)  $\zeta = 0$ ,  $\alpha = 10^\circ$  (b)  $\zeta = 0.03$ ,  $\alpha = 10^\circ$  (c)  $\zeta = 0$ ,  $\alpha = 20^\circ$  (d)  $\zeta = 0.03$ ,  $\alpha = 30^\circ$



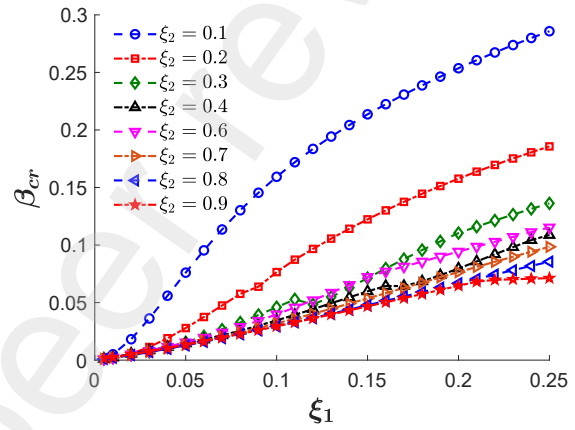
(a)



(b)

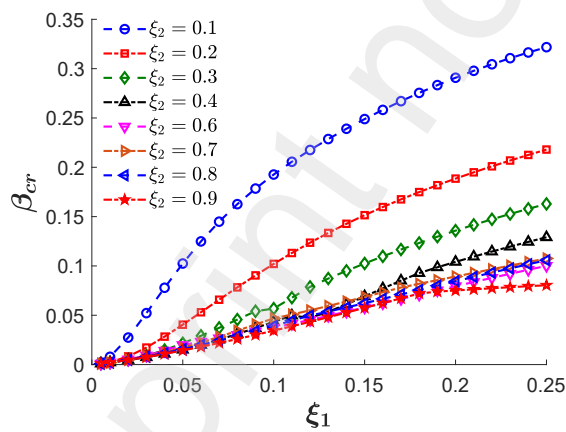


(c)

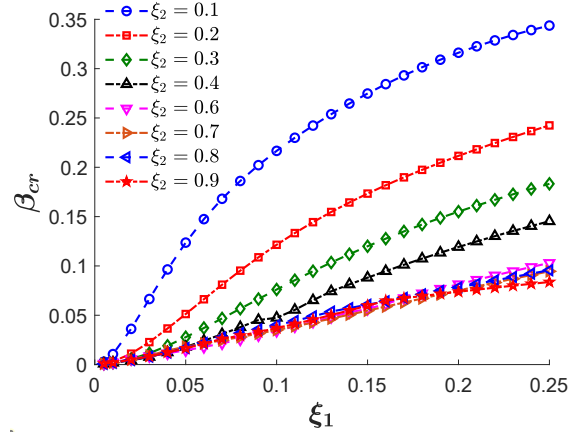


(d)

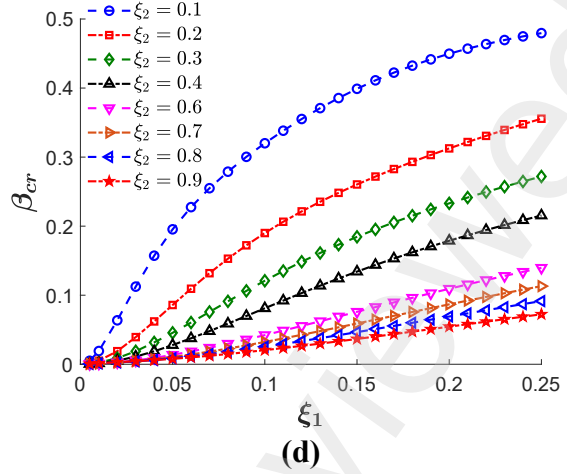
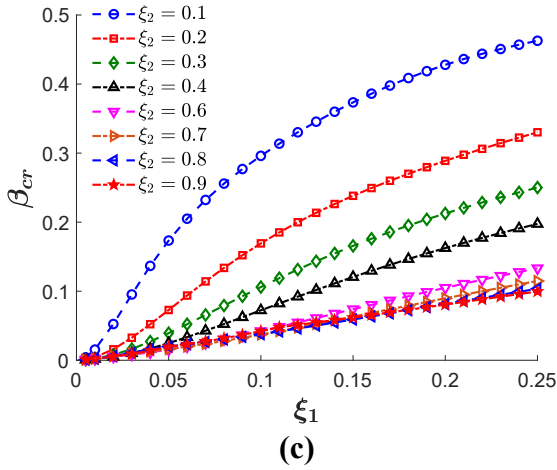
**Figure 16** Variation of  $\beta_{cr}$  with  $\xi_1$  for varying  $\xi_2$  for PFGM with  $\eta = 5$   
**(a)**  $\zeta = 0$ ,  $\alpha = 10^\circ$  **(b)**  $\zeta = 0.03$ ,  $\alpha = 10^\circ$  **(c)**  $\zeta = 0$ ,  $\alpha = 20^\circ$  **(d)**  $\zeta = 0.03$ ,  $\alpha = 30^\circ$



(a)

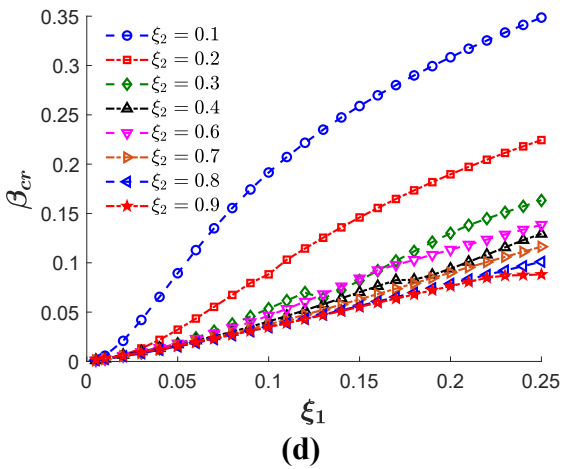
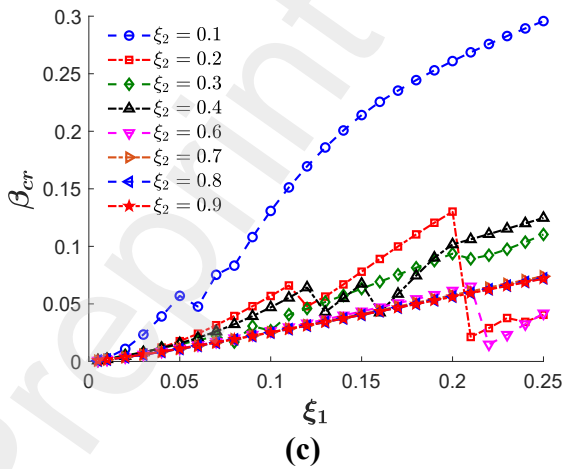
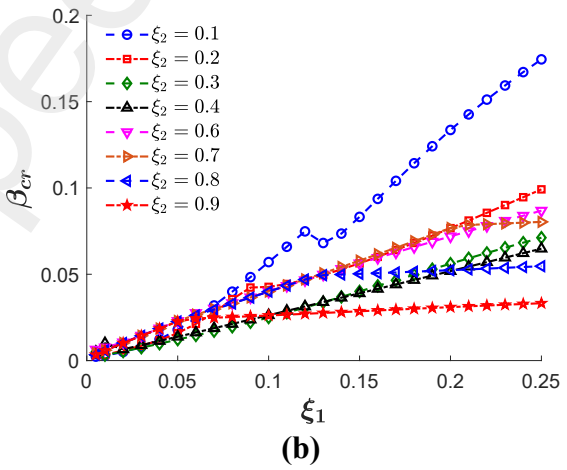
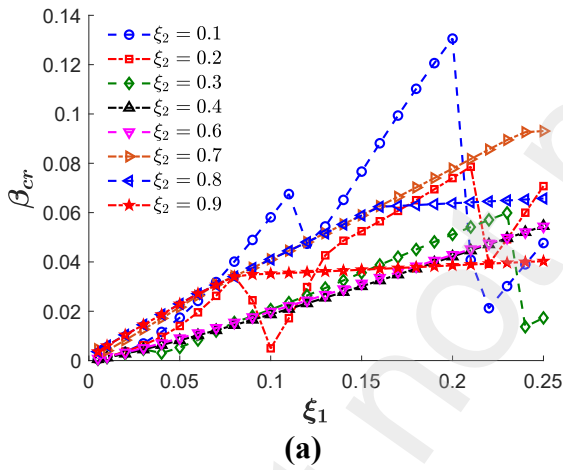


(b)



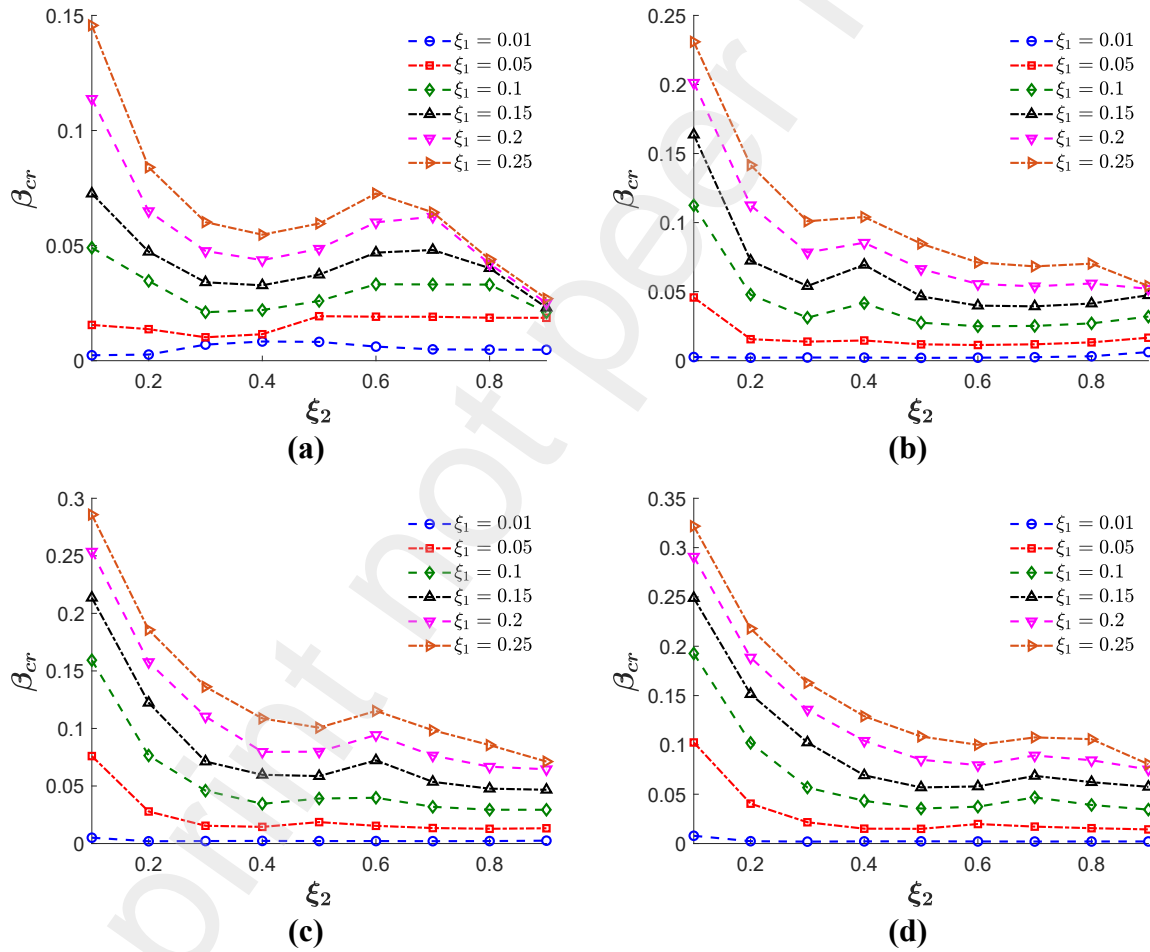
**Figure 17** Variation of  $\beta_{cr}$  with  $\xi_1$  for varying  $\xi_2$  for PFGM,  $\zeta = 0.03$   
**(a)**  $\eta = 5$ ,  $\alpha = 40^\circ$  **(b)**  $\eta = 5$ ,  $\alpha = 50^\circ$  **(c)**  $\eta = 1$ ,  $\alpha = 60^\circ$  **(d)**  $\eta = 1$ ,  $\alpha = 80^\circ$

Comparison between *Figure 15a-d* and *Figure 18a-d* show that all parameters being identical, the critical loads in the EFGM model are close to that of the PFGM model with  $\eta = 1$ .



**Figure 18** Variation of  $\beta_{cr}$  with  $\xi_1$  for varying  $\xi_2$  for EFGM  
**(a)**  $\zeta = 0$ ,  $\alpha = 10^\circ$  **(b)**  $\zeta = 0.03$ ,  $\alpha = 10^\circ$  **(c)**  $\zeta = 0$ ,  $\alpha = 20^\circ$  **(d)**  $\zeta = 0.03$ ,  $\alpha = 30^\circ$

Figure 19a-f present the variation of  $\beta_{cr}$  with varying  $\xi_2$  for different combination of the  $(\alpha, \xi_1, \eta, \zeta)$  values. For a semi-vertex angle ( $\alpha$ ) of the truncated conical shell less than  $40^\circ$  and thickness ratio ( $\xi_1$ ) greater than 0.1, the critical flutter load ( $\beta_{cr}$ ) first decreases up to a particular length parameter ( $\xi_2$ ) and then increases shortly before decreasing again. This reduction in the critical load after the rising part is because of a mode jump from a lower circumferential wave number to a higher mode, triggering the flutter. This is identical to the formation of an Arnold's tongue. These curves also merge for large  $\xi_2$  values because the non-dimensional critical load attains constant value for changing  $\xi_1$  as seen before. For other parametric values, the critical load decreases monotonically with increasing  $\xi_2$ .



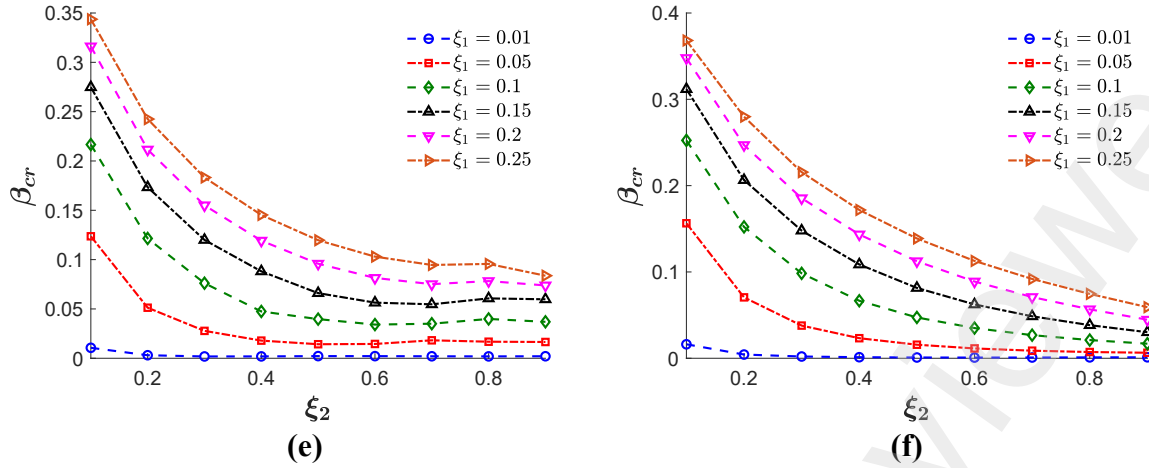


**Figure 19** Variation of  $\beta_{cr}$  with  $\xi_2$  for varying  $\xi_1$  for PFGM,  $\eta = 5$ ,  $\zeta = 0.03$

(a)  $\alpha = 10^\circ$  (b)  $\alpha = 20^\circ$  (c)  $\alpha = 30^\circ$  (d)  $\alpha = 40^\circ$  (e)  $\alpha = 50^\circ$  (f)  $\alpha = 80^\circ$

#### 4. Summary and Conclusions

Stability behavior of FG truncated conical shells under follower force is presented by adopting a simple, yet efficient finite element formulation. The analyses explain the effects of the shell geometry and material properties on the critical flutter load, expressed in terms of a number of non-dimensional parameters involving the geometry and material properties. The FG truncated conical shell is assumed to be clamped at the smaller edge and free at the larger edge and is subjected to a uniformly distributed follower force at the free end. Power-law and exponential functional gradations across the shell thickness are considered. A three-noded Lagrangian element discretization is adopted along the meridian whereas harmonic basis is employed along the circumference for approximating the displacement field. A mesh convergence study is carried out to ascertain the suitable mesh size for discretization. The analysis is verified against the free vibration characteristics reported in earlier study.

Mass and stiffness proportional damping is considered. The analysis under follower force reveals flutter type instability in undamped shells, whereas both flutter and divergence instabilities occur for damped shells. The flutter happens for a lower magnitude of the follower force as compared to divergence. A number of erratic weak instabilities are also observed for undamped and lightly damped shells, manifested as drastic drops in the load from the general trend of the critical flutter load in the parameter space. Long shells with small semi-vertex angles are relatively less susceptible to weak instabilities even though they exhibit a much lower critical load. It becomes imperative to perform instability analysis for undamped and lightly damped short truncated conical shells subjected to follower forces. The stability of the shell is sensitive to even a slight perturbation in its geometric properties.

Structural damping enhances stability by increasing the magnitude of the critical load, but its effect beyond three percent damping is mostly negligible.

For a given circumferential wave numbers, the locus of a pair of identical coalescing (longitudinal) modes are found to result into smooth curves. The lowest of all these critical loads gives the general variation of the critical load in the parameter space. The critical flutter load for PFGM shell decreases monotonically with increasing volume fraction index. The largest and smallest critical loads are for homogeneous shells with aluminum and zirconia, respectively. The non-dimensional critical load remains constant beyond a particular thickness parameter ( $\xi_1$ ) for long shells with low semi-vertex angles. The critical load decreases for increasing length parameter ( $\xi_2$ ) except for small semi-vertex angles and thickness parameters ( $\xi_1$ ) greater than 0.1. In the latter case, the critical load drops initially, followed by an increasing trend before reducing again.

## References

- AminYazdi, A. 2021. Flutter of geometrical imperfect functionally graded carbon nanotubes doubly curved shells. *Thin-Walled Structures* 164, p. 107798. doi: 10.1016/j.tws.2021.107798.
- Barsoum, R.S. 1971. Finite element method applied to the problem of stability of a non-conservative system. *International Journal for Numerical Methods in Engineering* 3(1), pp. 63–87. doi: 10.1002/nme.1620030110.
- Bhangale, R.K., Ganesan, N. and Padmanabhan, C. 2006. Linear thermoelastic buckling and free vibration behavior of functionally graded truncated conical shells. *Journal of Sound and Vibration* 292(1–2), pp. 341–371. doi: 10.1016/J.JSV.2005.07.039.
- Chi, S.H. and Chung, Y.L. 2006. Mechanical behavior of functionally graded material plates under transverse load-Part I: Analysis. *International Journal of Solids and Structures* 43(13), pp. 3657–3674. doi: 10.1016/J.IJSOLSTR.2005.04.011.
- Chopra, A.K. 2012. *Dynamics of Structures: Theory and Applications to Earthquake Engineering*. Upper Saddle River, N.J.: Prentice Hall.
- Flügge, W. 1966. *Stresses in shells*. New York: Springer-Verlag.
- Ibrahim, H.H., Tawfik, M. and Al-Ajmi, M. 2008. Non-linear panel flutter for temperature-dependent functionally graded material panels. *Computational Mechanics* 41(2), pp. 325–334. doi: 10.1007/s00466-007-0188-4.
- Ibrahim, H.H., Yoo, H.H. and Lee, K.-S. 2009. Supersonic Flutter of Functionally Graded Panels Subject to Acoustic and Thermal Loads. *Journal of Aircraft* 46(2), pp. 593–600. doi: 10.2514/1.39085.

- Irie, T., Yamada, G. and Tanaka, K. 1984. Natural frequencies of truncated conical shells. *Journal of Sound and Vibration* 92(3), pp. 447–453. doi: 10.1016/0022-460X(84)90391-2.
- Jung, W.Y. and Han, S.C. 2014. Transient analysis of FGM and laminated composite structures using a refined 8-node ANS shell element. *Composites Part B: Engineering* 56, pp. 372–383. doi: 10.1016/J.COMPOSITESB.2013.08.044.
- Kayran, A. and Vinson, J.R. 1990. Free vibration analysis of laminated composite truncated circular conical shells. *AIAA Journal* 28(7), pp. 1259–1269. doi: 10.2514/3.25203.
- Kim, J.H. and Kim, H.S. 2000. A study on the dynamic stability of plates under a follower force. *Computers & Structures* 74(3), pp. 351–363. doi: 10.1016/S0045-7949(99)00023-1.
- Koizumi, M. 1997. FGM activities in Japan. *Composites Part B: Engineering* 28(1–2), pp. 1–4. doi: 10.1016/S1359-8368(96)00016-9.
- Koizumi, M. and Niino, M. 1995. Overview of FGM Research in Japan. *MRS Bulletin* 20(1), pp. 19–21. doi: 10.1557/S0883769400048867.
- Langthjem, M.A. and Sugiyama, Y. 2000. Dynamic stability of columns subjected to follower loads: A survey. *Journal of Sound and Vibration* 238(5), pp. 809–851. doi: 10.1006/JSVI.2000.3137.
- Leissa, A.W. 1993. *Vibration of Shells*. Washington, D.C.: Acoustical Society of America.
- Liew, K.M., Ng, T.Y. and Zhao, X. 2005. Free vibration analysis of conical shells via the element-free kp-Ritz method. *Journal of Sound and Vibration* 281(3–5), pp. 627–645. doi: 10.1016/J.JSV.2004.01.005.
- Mahmoudkhani, S., Haddadpour, H. and Navazi, H.M. 2010. Supersonic flutter prediction of functionally graded conical shells. *Composite Structures* 92(2), pp. 377–386. doi: 10.1016/J.COMPSTRUCT.2009.08.018.
- Malekzadeh, P., Fiouz, A.R. and Sobhrouyan, M. 2012. Three-dimensional free vibration of functionally graded truncated conical shells subjected to thermal environment. *International Journal of Pressure Vessels and Piping* 89, pp. 210–221. doi: 10.1016/J.IJPVP.2011.11.005.
- Muc, A. and Flis, J. 2021. Flutter characteristics and free vibrations of rectangular functionally graded porous plates. *Composite Structures* 261, p. 113301. doi: 10.1016/J.COMPSTRUCT.2020.113301.
- Novozhilov, V.V. 1964. *Thin shell theory*. Groningen: P. Noordhoff.
- Park, S.H. and Kim, J.H. 2000. Dynamic stability of a completely free circular cylindrical shell subjected to a follower force. *Journal of Sound and Vibration* 231(4), pp. 989–1005. doi: 10.1006/JSVI.1999.2319.
- Reddy, J.N. 2000. Analysis of functionally graded plates. *International Journal for Numerical Methods in Engineering* 47(1–3), pp. 663–684. doi: 10.1002/(SICI)1097-0207(20000110/30)47:1/3<663::AID-NME787>3.0.CO;2-8.



Sabri, F. and Lakis, A.A. 2013. Efficient Hybrid Finite Element Method for Flutter Prediction of Functionally Graded Cylindrical Shells. *Journal of Vibration and Acoustics* 136(1). Available at: <https://doi.org/10.1115/1.4025397>.

Sanders, J.L. 1959. *An improved first-approximation theory for thin shells*. Washington, D.C.: NASA.

Shu, C. 1996. An efficient approach for free vibration analysis of conical shells. *International Journal of Mechanical Sciences* 38(8–9), pp. 935–949. doi: 10.1016/0020-7403(95)00096-8.

Simitses, G. and Hodges, D.H. 2006. *Fundamentals of Structural Stability*. Burlington, USA: Butterworth-Heinemann Publications, Elsevier.

Soedel, W. 2004. *Vibrations of Shells and Plates*. 3rd ed. Boca Raton: CRC Press.

Su, Z., Wang, L., Sun, K. and Wang, D. 2019. Vibration characteristic and flutter analysis of elastically restrained stiffened functionally graded plates in thermal environment. *International Journal of Mechanical Sciences* 157–158, pp. 872–884. doi: 10.1016/J.IJMECSCI.2019.05.028.

Sun, Y., Song, Z., Ma, W. and Li, F. 2021. Influence mechanism of lumped masses on the flutter behavior of structures. *Aerospace Science and Technology* 111, p. 106524. doi: 10.1016/J.AST.2021.106524.

Tong, L. 1993. Free vibration of composite laminated conical shells. *International Journal of Mechanical Sciences* 35(1), pp. 47–61. doi: 10.1016/0020-7403(93)90064-2.

Torki, M.E., Kazemi, M.T., Haddadpour, H. and Mahmoudkhani, S. 2014a. Dynamic stability of cantilevered functionally graded cylindrical shells under axial follower forces. *Thin-Walled Structures* 79, pp. 138–146. doi: 10.1016/J.TWS.2013.12.005.

Torki, M.E., Kazemi, M.T., Reddy, J.N., Haddadpoud, H. and Mahmoudkhani, S. 2014b. Dynamic stability of functionally graded cantilever cylindrical shells under distributed axial follower forces. *Journal of Sound and Vibration* 333(3), pp. 801–817. doi: 10.1016/J.JSV.2013.09.005.

Tornabene, F., Viola, E. and Inman, D.J. 2009. 2-D differential quadrature solution for vibration analysis of functionally graded conical, cylindrical shell and annular plate structures. *Journal of Sound and Vibration* 328(3), pp. 259–290. doi: 10.1016/J.JSV.2009.07.031.

Vlasov, V.Z. 1964. *General theory of shells and its applications in engineering*. Washington, D.C.: NASA.

Wei, J., Song, Z. and Li, F. 2020. Superior aeroelastic behaviors of axially functional graded cylindrical shells in supersonic airflow. *Journal of Fluids and Structures* 96, p. 103027. doi: 10.1016/J.JFLUIDSTRUCTS.2020.103027.

Zhao, X. and Liew, K.M. 2011. Free vibration analysis of functionally graded conical shell panels by a meshless method. *Composite Structures* 93(2), pp. 649–664. doi: 10.1016/J.COMPSTRUCT.2010.08.014.

Zhou, X., Wang, Y. and Zhang, W. 2021. Vibration and flutter characteristics of GPL-reinforced functionally graded porous cylindrical panels subjected to supersonic flow. *Acta Astronautica* 183, pp. 89–100. doi: 10.1016/J.ACTAASTRO.2021.03.003.